Department of Physics and Astronomy
Heidelberg University

Bachelor Thesis in Physics
submitted by

Philipp Martin Weingardt

born in Nürtingen (Germany)

2025

Calibration of an Absorption Imaging System Considering Multiple Photon Scattering

This bachelor thesis has been carried out by
Philipp Martin Weingardt
at the Kirchhoff institute for physics in Heidelberg
under the supervision of
Prof. Dr. Markus K. Oberthaler

Abstract

This thesis demonstrates the implementation of an improved calibration method for the absorption imaging system of a Bose-Einstein condensate of potassium-39. The calibration, which accounts for multiple scattering of photons in the atomic cloud, is tested in a variety of settings. First, two calibration schemes are compared: one where the total number of scattered photons per atom is kept constant, and another where imaging pulse duration is kept constant. Also, the influence of different density gradients on the calibration is studied. In order to investigate the validity of the experimental results, a numerical model for photon scattering is used and qualitative agreement with the experiment is found. The resulting calibration provides a more consistent measured atom number across different densities, imaging intensities, and imaging pulse durations.

Zusammenfassung

Diese Arbeit implementiert eine verbesserte Kalibrationsmethode eines Absorption Imaging Systems, verwendet zur Abbildung eines BECs in einem Kalium-39 Experiment. Diese Kalibrationsmethode berücksichtigt die Mehrfachstreuung von Photonen in der Atomwolke und wird für verschieden experimentelle Szenarien getestet. Zwei Kalibrationsansätze werden verglichen: einer, bei dem die Gesamtzahl der gestreuten Photonen pro Atom konstant gehalten wird, und ein weiterer, bei dem die Laserpulsdauer konstant gehalten wird. Weiterhin wird der Einfluss verschiedener Dichtegradienten auf die Kalibration untersucht. Um die Gültigkeit der experimentellen Ergebnisse zu untersuchen, wird ein numerisches Modell zur Simulation der Photonenstreuung verwendet und die qualitative Übereinstimmung mit den experimentellen Ergebnissen gezeigt. Die sich daraus ergebende Kalibration liefert eine konsistentere Anzahl von Atomen für unterschiedliche Dichten, Laserintensitäten und Laserpulsdauern.

Contents

The question is not what you look at, it's what you see.

HENRY DAVID THOREAU

Chapter 1

Introduction

Bose-Einstein Condensates (BEC) are a versatile tool for studying a wide range of physical phenomena, from pattern formation to cosmological particle production. While there are many methods to extract information from such systems, a key observable is a spatially resolved density distribution of the atomic cloud. One method for measuring density distributions is absorption imaging, which can provide high resolution, in-situ measurements of atomic densities.

The basic principle of absorption imaging involves illuminating atoms with light resonant to a specific atomic transition. First an image with the atomic cloud is taken (atom image), followed by another image of the imaging light on the camera without atoms (reference image). The difference in intensity reveals the number of scattered photons in a spatially resolved manner. To interpret this as a density distribution, one must consider the classical effects of absorption, such as the cross section specific to the atoms, as well as the exponential attenuation of the light intensity as it passes through the atomic cloud. Beyond that, also quantum effects, such as the saturation of the atomic transition and the detuning of the probe light from resonance must be considered. Reinaudi et al. [1] proposed a method to address this challenge, providing a description of the underlying processes of absorption and saturation of atomic transitions. Based on this work, absorption imaging systems could be effectively calibrated. A calibration following this idea is currently used for the experiment described in this thesis, as detailed in [2].

One assumption made in the widely used Reinaudi framework is that photons are lost from the cloud after being reemitted by an atom. While this is true in dilute clouds, in dense clouds, photons reemitted from one atom can influence the absorption of neighbouring atoms. This additional effect is considered in the works of Vibel et al. [3] and Veyron et al. [4]. Photons that have been scattered by an atom can still contribute to the light intensity and saturation of the transition and can be scattered again with a small but finite probability. Because this effect depends on the atomic density, it can introduce an apparent dependence of the total atom number on the shape of the density distribution.

In this thesis, the implementation of a new imaging calibration is presented that takes density-dependent processes into account. This achieves a significant improvement for the number of atoms measured, independent of cloud size and the imaging intensity.

The first chapter presents the theoretical foundations of absorption imaging, an overview of the experimental setup, and the simulation method used for the 1D-model. The second chapter describes the implementation of the density-dependent calibration method. It presents results for two techniques used to calibrate the imaging system: one where the number of scattered photons per atom is kept constant while imaging pulse length and intensity are varied, and another where pulse length is kept constant, but imaging intensity is varied. It is analysed how different density distributions — homogenous or linear density distributions in the cloud — influence the calibration. The results comparing both calibrations are presented, showing a more stable number of atoms by using the new calibration. The third chapter introduces a 1D model that analyses the effects of multiple scattering at different atomic densities and the simulation results provide a qualitative comparison to the calibration.

Chapter 2

Theoretical and Experimental Fundamentals

In this chapter, an introduction into the theoretical framework underlying the work of this thesis will be provided. The contents of this chapter cover the absorption of light by the atoms, the description of the absorption by the optical Bloch equations (OBE), leading to the Beer-Lambert law and the necessary considerations for the calibration of the absorption imaging system. Then a basic description of a Bose-Einstein Condensate and the properties of Potassium-39, the atom used in the experiment this work is performed on (the BECK-experiment). Finally, the experimental setup of the BECK experiment is discussed.

2.1 Absorption Imaging in Quantum Gases

The primary imaging system used in the BECK experiment is absorption imaging, which enables visualization of the atomic cloud. The absorption of light by atoms is governed by the optical Bloch equations.

2.1.1 Optical Bloch Equations and Beer-Lambert Law

The absorption of laser light by the atomic cloud follows the model presented in [1] and [5], describing each atom as an effective two-level system, and including the effect of saturation.
The two levels considered are the ground state and an excited state, an external electromagnetic field with the resonance frequency of this transition ω_0 excites the atoms. On resonance the atom population oscillates between the two states, in a process known as Rabi cycling, with the cycling frequency Ω called Rabi frequency. This cycling can be interrupted by spontaneous decay from the excited state back to the ground state, emitting a photon.
This spontaneous behaviour is modelled by an exponential decay of the atom population of the excited state with the rate Γ. This is the natural linewidth of the transition and corresponds to a natural lifetime of $\tau = \frac{1}{\Gamma}$. The time evolution of the atomic population is described by the optical Bloch equations. Incoherent decay from the excited state leads to a loss of coherence in the Rabi oscillations, limiting the excited-state population ρ_{ee} to be at most equal to the ground-state population ρ_{gg}.

The difference in population between the two states is given by

$$w = \rho_{gg} - \rho_{ee} = \frac{1}{1+s}, \tag{2.1}$$

where s is the off-resonance saturation parameter

$$s = \frac{s_0}{1 + (2\delta/\Gamma)^2}, \tag{2.2}$$

with $\delta = \omega - \omega_0$ as the detuning and s_0 as the on-resonance saturation parameter:

$$s_0 = \frac{2|\Omega|^2}{\Gamma^2} = \frac{I}{I_{sat}}. \tag{2.3}$$

The on-resonance saturation intensity I_{sat} is defined by the condition $\Omega = \Gamma$, and is given by:

$$I_{sat} = \frac{\hbar}{12\pi c^2}\omega^3\Gamma. \tag{2.4}$$

For the imaging transition this is [6]: $I_{sat} = 17.479\frac{W}{m^2}$.

The saturation of the transition poses a limit to the number of photons that can be scattered by the cloud. The total scattering rate is derived from the population of the excited state and the decay rate using equation (2.3) and (2.2), and taking into consideration that the total population is normalized to one:

$$\gamma = \Gamma\rho_{ee} = \frac{\Gamma}{2}\frac{s_0}{1 + s_0 + (2\delta/\Gamma)^2}. \tag{2.5}$$

To infer an atom number from the number of absorbed photons the cloud is modelled as an effective two-level system including the above described effect of saturation. The reduction of the intensity in the cloud can be described by

$$\frac{dI}{dz} = -\hbar\omega\gamma n, \tag{2.6}$$

with n the number of atoms in the cloud. Using (2.5) and in a second step assuming the used light to be on resonance ($\delta = 0$, $\omega = \omega_0$) and employing (2.3) this results in the following expression for the intensity reduction:

$$\frac{dI}{dz} = -\hbar\omega\frac{\Gamma}{2}\frac{s_0}{1 + s_0 + (2\delta/\Gamma)^2}n = -\hbar\omega_0\frac{\Gamma}{2}\frac{I/I_{sat}}{1 + I/I_{sat}}n. \tag{2.7}$$

Now the resonant scattering cross section is introduced

$$\sigma_0 = \frac{\hbar\omega_0\Gamma}{2I_{sat}}, \tag{2.8}$$

and can recover Beer's law including saturation from (2.7)

$$\frac{dI}{dz} = -\sigma_0 n\frac{1}{1 + I/I_{sat}}I. \tag{2.9}$$

The column density of the atomic cloud can be calculated by solving the differential equation to get the final result:

$$n_c = \int n dz = \frac{1}{\sigma_0}\left[ln\left(\frac{I_0}{I_1}\right) + \frac{I_0 - I_1}{I_{sat}}\right], \tag{2.10}$$

where I_0 is the intensity of the light on the reference picture taken without atoms and I_1 is the imaging light intensity measured by the CCD with the atoms.

2.1.2 Effective Saturation Parameter α

The focus of this thesis is the calibration of the absorption imaging system to improve atomic density measurements. This calibration accounts for deviations from the idealized two-level system by introducing an effective saturation intensity:

$$I_{sat}^{\text{eff}} = \alpha I_{sat}, \tag{2.11}$$

where I_{sat} is the saturation intensity for the idealized two-level system. The parameter α originally accounted for effects of beam polarization, the specific structure of the excited states and the different ground state Zeeman sub-levels [1], and therefore this parameter needs to be experimentally calibrated. The system is then described by the effective value of the saturation intensity and the effective cross section

$$\sigma_0^{\text{eff}} = \frac{\hbar\omega_0\Gamma}{2\alpha I_{sat}}, \tag{2.12}$$

now equation (2.10) can be rewritten as:

$$n_c = \int n dz = \frac{\alpha}{\sigma_0}\left[ln\left(\frac{I_0}{I_1}\right) + \frac{I_0 - I_1}{\alpha I_{sat}}\right] = \frac{1}{\sigma_0}\left[\alpha \cdot ln\left(\frac{I_0}{I_1}\right) + \frac{I_0 - I_1}{I_{sat}}\right] \tag{2.13}$$

While the column density is used for calculating an actual number of atoms, for the following considerations on the absorption of laser light predominantly the dimensionless optical density will be used:

$$od = \alpha \cdot ln\left(\frac{I_0}{I_1}\right) + \frac{I_0 - I_1}{I_{sat}}. \tag{2.14}$$

A total number of atoms in the cloud can be calculated by summing over the column density multiplied with the area of each pixel. In terms of the optical density the following equation is obtained:

$$N = \frac{A}{\sigma_0}\sum_i^{ROI} od_i, \tag{2.15}$$

where A is the area of each pixel and od_i is the optical density in the i-th pixel in the region of interest (ROI).

2.2 Multiple Scattering

The following investigations aim to achieve a more precise calibration of the absorption imaging system using the technique presented above. This is motivated by results pointing towards the influence of multiple scattering effects considered in [3] as an explanation for the experimental results and used in [7] to model the trend of the effective saturation parameter $\alpha^*(od)$. Thus, in this section the influence of multiple scattering on the properties relevant for absorption imaging will be briefly discussed, which will aid in interpreting the results produced over the course of this work.

The absorption and re-emittance is the key pillar of absorption imaging. If happening sufficiently often, the absorption of photons by atoms leads to a saturation of the transition of the atom. This forces a non-linear response of the atom to more incident photons. Consequently, the probability of further photon absorption decreases once the saturation limit is reached. While in the original model photons were considered lost from the atomic cloud, in the experiment, it is possible that rescattered photons contribute to the saturation of a second atom's transition. This effect is expected to scale with the number of atoms (thus the atomic/optical density) imaged, because more surrounding atoms account for a higher likelihood of scattered photons being re-absorbed. The result is saturation at lower laser intensities in regions of higher atomic density compared to regions with lower density but exposed to the same intensity.

The saturation as described above, can be understood as a decrease of the cross section of an atom for every next photon incident on the atom. The saturation at lower intensities is captured by the saturation parameter α^* which increases with optical density. Since $I_{sat}^{\text{eff}} = \alpha^* I_{sat}$ and $\sigma_0^{\text{eff}} \propto 1/\alpha^*$, an increase in α^* corresponds to a smaller effective atomic cross section. The understanding of the increase in I_{sat}^{eff} is not as intuitive, but can be seen as a measure for a regime of higher saturation and equally a non-linear response of the atoms at a lower laser intensity. This suggests that an increase in I_{sat}^{eff} means that more intensity is needed to achieve the same degree of non-linearity in the atomic response.

2.3 Calibration

Typically, experimental systems use a global calibration for α. Recent experimental and numerical evaluations, have shown that higher order effects of multiple scattering (MS) make this global calibration insufficient for describing clouds with widely varying densities. High cloud densities show different transmission than low ones, and this can be incorporated with a density-dependent α.

A new approach taking these effects into account is presented in [3], accounting for density-dependent changes in absorption behaviour, which influence the effective saturation intensity dependent of the atomic/optical density. A more detailed theoretical study of MS, as the cause of this phenomenon can be found in [4].
This density dependent (local) approach to the calibration forms the basis for this thesis. Therefore, in the following section, the previously used (global) method of calibration is discussed briefly, and the new local calibration technique for α^* for different optical densities is presented.

2.3.1 Global Calibration

The originally used calibration technique is based on the assumption that α can be estimated for the whole atomic cloud by minimizing the effect of different imaging intensities on the total atom number. This is comparable to the method presented in [1], but aims to minimize the variation in total atom number, rather than in peak column density, across different imaging intensities.
This *original* method employed in the experiment is detailed in [8]. In this work theoretical predictions were made for the value of I_{sat}^{eff} in the BECK experiment. The coupled four-level system is modelled as two independent two-level systems coupled via spontaneous decay, each with the same effective saturation intensity I_{sat}. It is assumed that no coherence builds up and the two systems can be described independently and therefore depend on the laser intensity ratio used for the two transitions $r = I_{Repumper}/I_{tot}$ ($I_{tot} = I_{Cooler} + I_{Repumper}$) . The necessity to use two transitions is explained in section 2.5.2.
The final analytical prediction of I_{sat}^{eff} is given by:

$$I_{sat}^{\text{eff}} = \frac{I_{sat}}{2r(1-r)} \tag{2.16}$$

The result for the optimal ratio of $r = 0.5$ for the present setup predicts an alpha value of $\alpha = 2$. The experimental calibration is performed by calculating $n_c\sigma_0^{\text{eff}}$ for measurements of an atomic cloud prepared identically, but imaged with varying total light intensities I_{tot} for the imaging light. With the right α chosen, the column density should remain constant for different imaging intensities, as the atom number stays constant. The calculation is therefore performed for different values of α and the optimal value for α was found to be $\boldsymbol{\alpha_{global} = 7.3}$. This is the calibration previously used.

2.3.2 Local Calibration

The *local* calibration method proposed by [3] attempts to account for density-dependent modifications in the absorption process. The calibration is thus performed in a more refined manner.
An atomic cloud is again prepared with a radially symmetric density gradient, rather than a uniform density profile. The cloud is prepared in the same way for different total imaging intensities. The number of absorbed photons per atom N_{abs} is kept constant and thus with increasing total imaging intensity the duration of the imaging pulses t_{pulse} is decreased. The number of absorbed photons per atom is kept constant because the scattering of the photons leads to a momentum transfer giving rise to a Doppler shift perceived by the atoms, acting as a effective detuning of the resonance frequency. The constant number of photons scattered per atom should minimize the additional effect of the Doppler shift.

The Doppler Shift induced on the atoms leads to a larger detuning between the laser frequency and the frequency of the corresponding transition, due to changes in the momentum of the atoms. Therefore the efficiency of the absorption of photons by the atoms changes. This assumption is also critically evaluated by performing calibrations with fixed imaging durations for comparison.

The pictures obtained from these measurements are further processed using elliptical masks to segment regions of approximately uniform optical density *od*. The optical density *od* is defined as in equation (2.14).
The calibration is now performed for each region by calculating the $\ln\left(\frac{I_0}{I_1}\right)$ and $\frac{I_0-I_1}{I_{sat}}$ of every pixel individually and than averaging the results for every k-th region. By rearranging equation (2.14)

$$\left\langle \frac{I_0 - I_1}{I_{sat}} \right\rangle_k = \langle od \rangle_k - \alpha_k^* \left\langle \ln\left(\frac{I_0}{I_1}\right) \right\rangle_k , \tag{2.17}$$

the value of α^* for every region can be found. A linear fit is now applied to the averaged regions to determine α^* as the slope of the linear fit and *od* as the intercept.
To find a more general dependence of $\alpha^*(od)$ another linear fit is applied to the α_k^* values over the corresponding values of *od* and the relation for $\alpha^*(od)$ is obtained

$$\alpha^*(od) = \alpha_0 + \alpha' od. \tag{2.18}$$

This result can then be used for applying a calibrated α^* depending on the local optical density of each pixel for the corresponding value of N_{abs}/t_{pulse}. The α^* for every pixel is calculated by:

$$\alpha^* = \frac{\alpha_0 + \alpha' \frac{(I_0-I_1)}{I_{sat}}}{1 - \alpha' \ln\left(\frac{I_0}{I_1}\right)}. \tag{2.19}$$

The resulting value of *od* can be calculated directly from α_0 and α' and the measured I_0/I_1 intensities for every pixel:

$$od = \frac{\alpha_0 \ln\left(\frac{I_0}{I_1}\right) + \frac{I_0-I_1}{I_{sat}}}{1 - \alpha' \ln\left(\frac{I_0}{I_1}\right)}. \tag{2.20}$$

The source also demonstrates a linear dependence of α_0 and α' on N_{abs}, enabling a generalized calibration procedure valid across varying imaging parameters. Such a relation was also obtained to make a more general use of the calibration without calibrating for every specific value of N_{abs} or t_{pulse}.

An alternative method combines the global calibration method (2.3.1) with spatially resolved pixel-wise estimation of α [7]. In this method, again the criterion is used that, for the correct value of α^*, the optical density should be constant across varying imaging light intensities I_0. By evaluating the optical density at each pixel, a local α^* value is obtained, and a similar linear dependence of $\alpha^*(od)$ is observed. For clarity of notation, $\alpha^* = \alpha$ will be used, unless stated otherwise.

2.4 1D-Model

To theoretically model the relationship between α and od, simulations were performed following the approach of [4]. The authors propose a 1D-model for Multiple Scattering in dense atomic clouds. The 1D approximation, considering only the dimension along the imaging path through the cloud (z-axis), is justified under the condition of a homogeneous atomic distribution in the transverse plane.

Because of the homogeneity, there cannot be a net energy flux in the x/y-plane. All the scattering events are considered to be effectively redistributed in the z-direction. In addition, to take into account the effect of saturation by the imaging intensity, the effective cross section of the atoms is also considered under the influence of the intensity of the incoherent field of scattered photons. In the following the on-resonance saturation parameter beforehand used as s_0 is now used as $s_c = I/I_{sat}$ for the incident coherent imaging light. The forward/backward scattered incoherent light intensity is also used as a nondimensional saturation intensity parameter

$$s_i^{\pm} = \frac{I_i^{\pm}}{I_{sat}^{iso}} \tag{2.21}$$

With $I_{sat}^{iso} = \alpha_{iso} I_{sat}$ introducing a parameter α_{iso} accounting for the change in the isotropic cross section due to the polarization of the incoherently scattered light. Depending on the polarization properties, $\alpha_{iso} = 1$ for σ-polarized light and $\alpha_{iso} = 2.12$ for isotropic polarization [4].

The scattering rates for both coherent and total processes are derived from the optical Bloch equations and are given by:

$$R_{sca}^{(coh)} = \frac{\Gamma}{2} \frac{s_c}{\alpha + s_c} \tag{2.22}$$

$$R_{sca}^{(tot)} = \frac{\Gamma}{2} \frac{s_c}{(\alpha + s_c)^2} \tag{2.23}$$

Including the contribution of incoherently rescattered light modifies the scattering rates under an effective two-level system (TLS) ansatz:

$$R_{sca}^{(coh)} = \frac{\Gamma}{2} \frac{s_c}{\alpha_{\text{eff}} + s_c} \tag{2.24}$$

$$R_{sca}^{(tot)} = \frac{\Gamma}{2} \left(\frac{s_c}{\alpha_{\text{eff}} + s_c} + \frac{s_i}{\alpha_c + s_i} \right) \tag{2.25}$$

with the corrected scattering rates given by:

$$\begin{aligned} \alpha_{\text{eff}} &= \alpha(1 + s_i) \\ \alpha_c &= 1 + s_c \end{aligned} \tag{2.26}$$

By using $R_{sca}^{(inc)} = R_{sca}^{(tot)} - R_{sca}^{(coh)}$ one can obtain the following coupled differential equations for the coherent and incoherent saturation parameter:

$$\begin{aligned} \frac{ds_c}{dz} &= -n(z)\sigma_0 \frac{s_c}{1+s_c+s_i}, \\ \frac{ds_i^{(\pm)}}{dz} &= -\frac{n(z)\sigma_0^{iso}}{2}\left(\frac{s_i^{(\pm)} - s_i^{(\mp)}}{1+s_c+s_i} - \frac{s_c(s_c+s_i)}{(1+s_c+s_i)^2} - \frac{s_c}{(1+s_c+s_i)^2}\right). \end{aligned} \tag{2.27}$$

Here, σ_0^{iso} denotes the isotropic scattering cross-section, and s_i is the total incoherent saturation parameter in a step dz: $s_i = s_i^{(+)} + s_i^{(-)}$. In the weak saturation limit mostly coherent scattering is expected, in the high field limit the scattering follows a Mollow spectrum (see [9]) and is mostly incoherent. Incoherent fields have off-resonance spectral components. To account for them the assumption of an on-resonance spectrum with a reduced isotropic scattering cross section σ_{iso} is used.

The prefactor 1/2 in Eq. 2.27 reflects the equal probability of incoherent scattering in the $+z$ and $-z$ directions. The first term than describes the rescattering of the incoherent field, the second term accounts for temporally incoherent scattering of the coherent field, while the third term ensures energy conservation and accounts for spatially incoherent scattering of the coherent field. Further discussion on spatially and temporally incoherent scattering contributions is available in [4].

2.5 Experimental Implementation

After this theoretical endeavour, this section will briefly introduce the experimental setup and techniques used for the realization of the quasi-2D Bose Einstein Condensate of Potassium-39 (the BECK experiment). All measurements discussed later were performed using the BECK experiment, and the calibration is specific to this setup. In the second part an overview of the imaging setup is provided, building on the theoretical fundamentals described in section 2.1. A more in depth discussion of the setup can be found in [2]. Before discussing the experimental realization of the imaging process in detail, the properties of potassium, the closed optical cycle used at intermediate magnetic field, and the general description of Bose-Einstein condensation are examined.

2.5.1 Properties of Potassium ^{39}K

Absorption Imaging can be performed in diverse experimental setups, but the exact setup is dependent on the properties of the atoms used in the experiment. This section will shortly discuss the properties of Potassium-39, the atom used in the BECK experiment, focusing on the level scheme and the hyperfine structure of the atom under influence of an external magnetic field.

The energy eigenstates of a ^{39}K atom are determined by its fine and hyperfine structure. The single valence electron is described by ($\mathbf{L}$,L) and ($\mathbf{S}$,S) being the orbital angular momentum and spin with quantum number, respectively. These couple together to the total electronic angular momentum $\mathbf{J} = \mathbf{L} + \mathbf{S}$. The resulting fine structure is split in $J = 1/2$ and $J = 3/2$. By coupling of the nuclear spin $I = 3/2$ with J the total angular

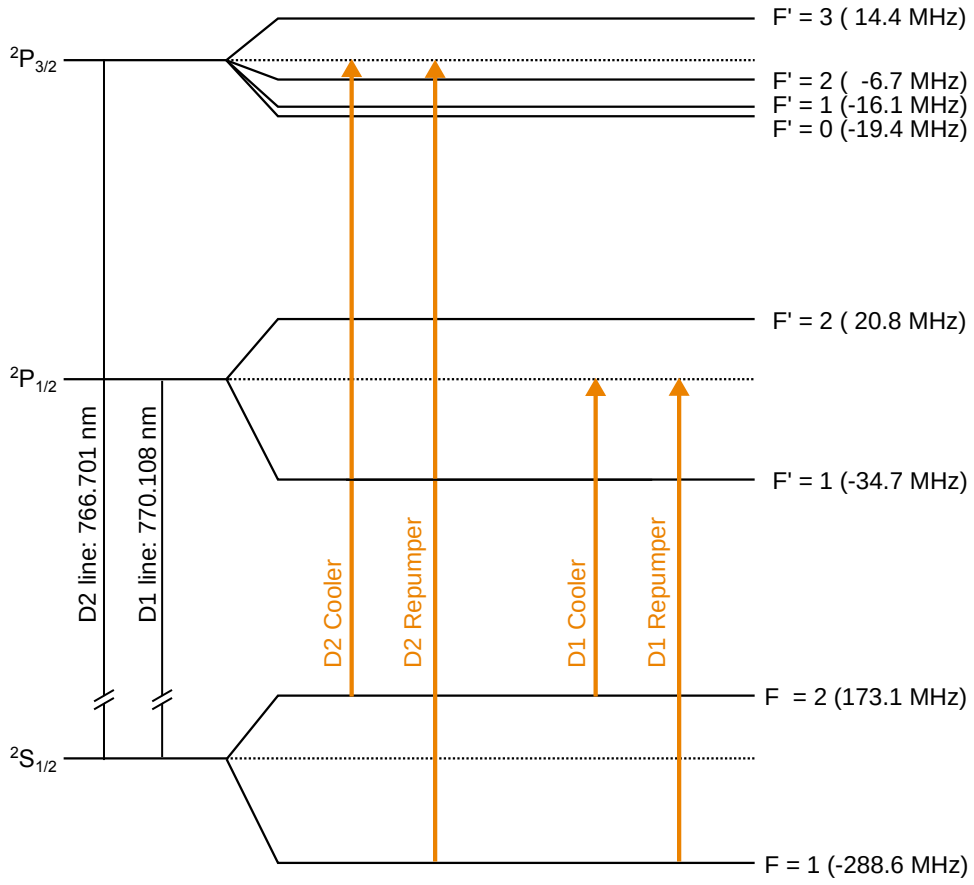

Figure 2.1: **Level scheme of potassium.** The ground state of potassium is the $^2S_{1/2}$ state, the first excited states due to fine structure splitting are $^2P_{1/2}$ and $^2P_{3/2}$. The corresponding transitions are called D1 and D2. Because of the coupling between the total electric angular momentum and nuclear spin the ground state is further split by hyperfine splitting (also the excited states are marginally split compared to their natural linewidth). The transition from the resulting upper/lower level of the ground state is called cooler/repumper transition. The figure is taken from [10].

momentum is formed $\mathbf{F} = \mathbf{J} + \mathbf{I}$. This leads to the hyperfine structure. At zero magnetic field the energy eigenstates are pure in the quantum number F. The level scheme of those energy eigenstates are shown in figure 2.1 for zero magnetic field.
The ground state of potassium is the $^2S_{1/2}$ state, the first excited states due to fine structure splitting are $^2P_{1/2}$ and $^2P_{3/2}$. The transition from the ground state to the excited states are called D1 and D2 transition. The hyperfine splitting is especially for the ground state significant. The transitions from the upper level ($F = 2$) are called cooler, the transitions from the lower level ($F = 1$) are called repumper. The terminology is chosen in analogy to the transitions of rubidium. At non zero, but low magnetic fields the eigenstates are in good approximation pure in the quantum number m_F, F, for higher magnetic fields the eigenstates are mixed in the quantum numbers m_J, m_I, as can be seen in figure 2.2.

2.5.2 Closed Optical Cycle

To achieve a high resolution imaging of the cloud it is desirable to scatter as many photons as possible in a short time frame. This requires a closed cycle transition to minimize losses to dark states not addressed by the imaging light.

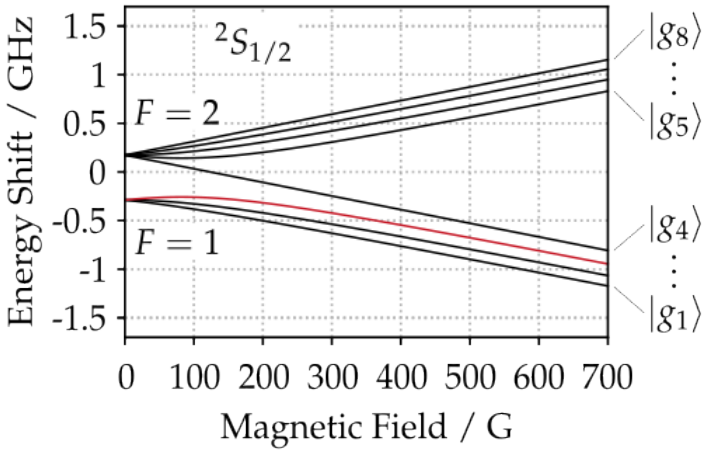

Figure 2.2: **Energy shifts of the hyperfine states with external magnetic field.** In the figure the shifts of the energy levels of the ground state $^2S_{1/2}$ with increasing magnetic field are shown. At the high magnetic field strengths depicted, the states are not any more pure in m_F, but become pure in the m_J, m_I-basis. The states are numbered as shown on the right. The mostly used ground state for the BECK experiment is the state marked in red $|g_3\rangle$, which corresponds to the state $|g_-\rangle$ mentioned below. The figure is taken from [2].

Unfortunately, measurements are done with a external magnetic field present to control the scattering length of the condensate. This is done by using a so called Feshbach resonance. This phenomenon occurs when the energy of a bound state in an interatomic potential is comparable to the kinetic energy of the scattering atoms. By applying a magnetic field at this specific resonance the scattering length of particles can be tuned positive or negative. In the BECK experiment a homogenous magnetic field is applied

close to the Feshbach Resonance of Potassium-39 at approximately $B = 561.12 \pm 0.02$ G [11]. This broad Feshbach resonance allows for a wide range of scattering lengths to be experimentally accessed.

At the magnetic field around $B = 550$ G the eigenstates are not pure in m_F any more, but exhibit significant mixing in the quantum numbers m_J, m_I, representing the magnetic quantum number of the total angular momentum m_J and the nuclear spin m_I. This increases the number of energy levels and consequently the number of possible transitions between them. This is described by the Breit-Rabi formula [12], and the effect is shown in figure 2.2 for the ground state $^2S_{1/2}$. Unfortunately, reducing the magnetic field to a vanishing regime is not feasible, as this would require crossing multiple Feshbach resonances. As a result, a closed cycle transition has to be used at high magnetic field.

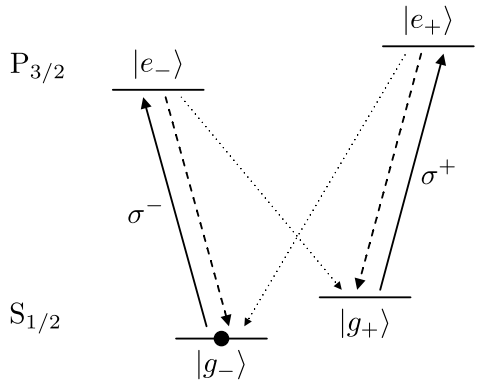

Figure 2.3: **Closed Optical Cycle of the imaging scheme.** In the figure the energy eigenstates used for the closed optical cycle are visualized. The ground state $|g_-\rangle$, the experiment is prepared in, is marked by the black dot. From there the first transition driven by σ^- polarized light is possible to the excited state $|e_-\rangle$. Between those states a Rabi cycle is driven. Unfortunately, when excited, the atoms are not confined to this transition, but can decay into the $|g_+\rangle$ state with a small probability. This would lead to a loss of atoms over time and is counteracted by driving a Rabi cycle to $|e_+\rangle$ including a small probability to decay back to $|g_-\rangle$, closing the optical cycle. Figure is taken from [8].

In the chosen closed cycle, the atoms are initially prepared in the state $|g_-\rangle = |m_J, m_I\rangle = |-1/2, -1/2\rangle$, the imaging light used for the D2 Transition with σ^- polarization excites the transition to the state $|e_-\rangle = |-3/2, -1/2\rangle$. However, decay from the excited state to $|g_+\rangle = |1/2, -3/2\rangle$ is possible. Relying solely on the σ^- transition would lead to a gradual loss of atoms into this dark state. Fortunately, the optical cycle can be closed by applying a second laser frequency driving the σ^+ transition to the state $|e_+\rangle = |+3/2, -3/2\rangle$, which can decay back to the state $|g_-\rangle$. The closed optical cycle is shown in figure 2.3.

An important question is the optimal intensity ratio between the two frequencies. This was addressed in [8] by varying the ratio between the two imaging transitions at constant total intensity. The optimal ratio was found to be $r = I_{\sigma^+}/(I_{\sigma^-} + I_{\sigma^+}) = 0.5$ (as mentioned earlier in section 2.3.1) yielding the maximum number of scattered photons. This value is used in subsequent experiments.

2.5.3 Bose-Einstein Condensate

The cloud of atoms in the BECK experiment forms a Bose-Einstein Condensate (BEC). A BEC is a state of matter occurring at temperatures close to absolute zero, with all atoms in the same ground state. If a system of N bosonic particles in a volume V for a density below $n = N/V$ is considered, only the two-body interactions become relevant. In the regime of weakly interacting particles, at low density and low temperature the interaction length r_0 is much smaller than the average distance between the particles $n^{-1/3}$. And this interparticle distance is smaller than the de Broglie wavelength of the particles. In this regime only s-wave scattering is relevant for two particle collisions and the interaction potential can therefore be replaced by a single interaction strength. This ultimately leads to the equation of motion being described by the Gross-Pitaevskii Equation, which is a non-linear Schrödinger equation ([13],[14]):

$$i\hbar\partial_t\Psi = \left[-\frac{\hbar^2}{2m}\nabla^2 + V(\mathbf{x}) + g|\Psi|^2\right]\Psi, \tag{2.28}$$

where Ψ is the wavefunction of the condensate, m is the mass of the bosons, $\hbar$ is the reduced Planck constant, $V(\mathbf{x})$ is the external potential and g is the interaction strength.

The general ansatz for the solution of the GPE is:

$$\Psi(\vec{x}, t) = \sqrt{n(\vec{x})}\exp(-i\mu_0 t/\hbar), \tag{2.29}$$

with μ_0 the chemical potential and the atom density $n = \Psi^*\Psi$. In the *Thomas-Fermi approximation* of dense clouds and a large trapping potential the kinetic term can be neglected. When using (2.29), this leads to:

$$n(\vec{x}) = \frac{\mu_0 - V(\vec{x})}{g}. \tag{2.30}$$

Therefore, the density is inversely proportional to the strength of the potential, this is used by the potential imprinted by the Digital Micromirror Device (DMD) to control the density profile in the atom cloud. explained in section 2.5.4. The study of the BEC in the BECK-experiment is predominantly done using absorption imaging to obtain a picture of the atomic cloud and draw conclusions about the density of the cloud, the experimental methods used to produce a BEC and image it are presented in the following section.

2.5.4 Cooling and Trapping

The heart of the BECK experiment is a vacuum chamber consisting of two chambers connected by a differential pumping stage. The left side of the chamber has an oven attached to it creating a thin background of Potassium atoms with a pressure of 10^{-7} to 10^{-8} mbar. From these atoms a 2D magneto-optical trap (MOT) is created resulting in a beam of pre-cooled atoms travelling to the science chamber and loading a 3D-MOT there. The science chamber is a glass cell, featuring access for the imaging and DMD (Digital Micromirror Device) light. The pressure in the 3D-MOT is below 10^{-11} mbar, ensuring a low heating rate and enabling the preparation of ultra-cold atomic samples. A further increase in density is achieved using a compressed MOT and cooling below the

Doppler-cooling limit is achieved via a grey molasses.

Following those steps, a magnetic field confines the atoms of the $|F, m_F\rangle = |1, -1\rangle$ state and compresses the cloud adiabatically. Since the scattering length is negative at zero magnetic field, immediate condensation of large clouds is not possible. Fortunately, the scattering length can be tuned by applying the homogenous magnetic field near the Feshbach resonance. During these steps, the atoms are loaded into an attractive optical dipole trap at 1064 nm.
The final step towards condensation is further cooling the atoms by evaporative cooling. This is achieved by lowering the depth of the dipole trap, which causes the hottest atoms to be lost, leaving the remaining atoms to cool down gradually. The gravitational pull is counteracted by a magnetic field gradient.

After successful condensation the atoms are confined in z-direction using the interference pattern of two lasers at 532 nm, creating a repulsive optical dipole trap. Between two minima of the interference pattern at a distance of 5 µm a harmonic trap is created resulting in a atom cloud with a width of approximately $\sigma_z = 0.4\mu m$ (for further information on the confinement by the pancake sheets see [10]). Through the confinement in this harmonic trap, quasi-two-dimensionality is achieved. The trap frequency is $\omega_x = 2\pi \times 1.5$ kHz. The temperature of the cloud is approximately $T = 20$ nK and the number of atoms is $N \approx 50000$.

During measurements, the interaction strength g can be tuned by manipulating the scattering length a via the homogenous magnetic field close to the Feshbach resonance. The external potential is spatially controlled by the DMD. This device consists of 2560×1600 micromirrors that can be individually turned on or off. The DMD is illuminated by a Gaussian laser beam at 532 nm, when the mirrors are turned on the light is projected on the atoms creating the external potential $V(\vec{x})$. This potential can be arbitrarily chosen, because the laser is strongly demagnified after the DMD. Because the spatial resolution of the objective is limited, 6×6 mirrors are unresolved in the plane of the atoms. Thus 36 levels of greyscale can be used to create differently shaped potentials. This was used in this project to imprint homogenous, linear and Gaussian density profiles.

2.5.5 Imaging system

The imaging setup is based on the absorption imaging technique described in section 2.1. It consists of two lasers at approximately 767 nm, illuminating the atomic cloud with resonant light. Absorption of resonant light heats the condensate, causing it to be destroyed during imaging. As a result, each measurement requires repeating the entire loading cycle. The light absorbed by the atoms is remitted in arbitrary directions. The light not absorbed by atoms (and light scattered in the direction of the objective of the camera) is then imaged with a CCD camera.
The CCD camera used is a ProEM camera, which serves as the primary imaging system in the experiment. The path of the imaging light is as follows. The laser is directed onto the glass cell containing the atomic cloud. The light transverses two lenses, to ensure the beam is collimated in the plane of the atomic cloud and the objective above the glass cell. After passing through the glass cell and the atomic cloud the light is collected by

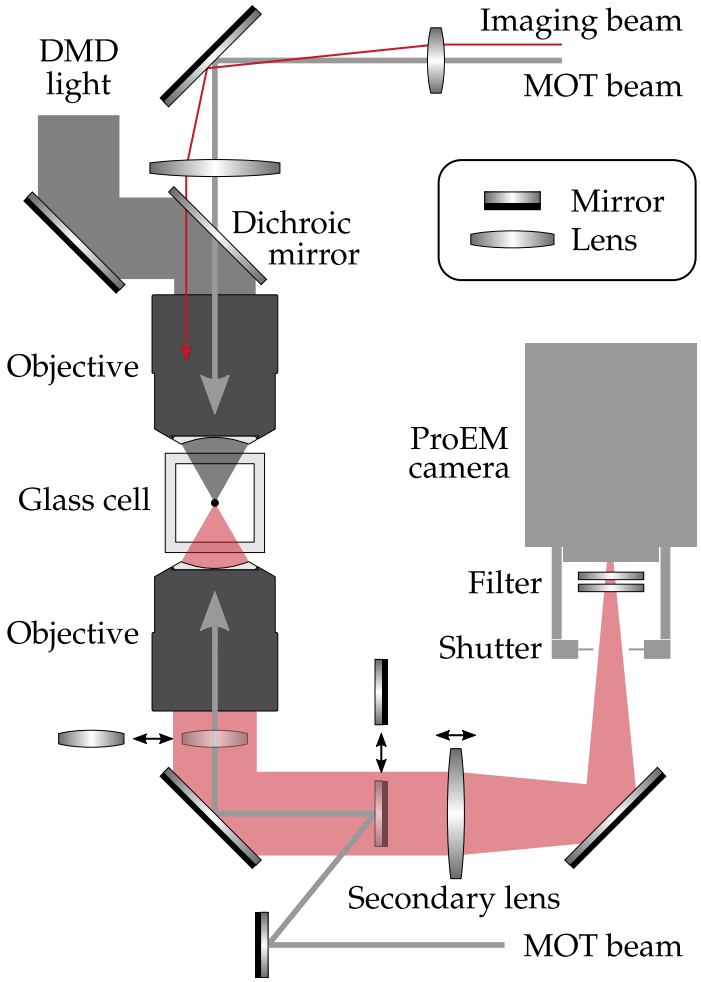

Figure 2.4: **Path of the imaging beam through the glass cell.** The path of the resonant laser used for absorption imaging is depicted in red. The light passes through a objective above the glass cell containing the atom cloud and is collected by a similar objective below the glass cell and imaged onto the camera. The figure also shows the path of the DMD light used to confine the atoms in various potentials. The figure is taken from [8]

another objective and focused onto the CCD camera. A sketch of the setup is presented in figure 2.4.

The process of collecting light on the CCD is complex, because two pictures are taken and cannot be read out quickly enough during a single imaging cycle. To address this, only 1024×1024 pixels out of the 1024×2048 total pixels of the ProEM camera are used to capture the picture. The other half is used to store the previously taken picture. The first image is transferred to the bottom half of the camera where it can be read out while the second image is being captured. The spatial calibration performed for this imaging system concludes a 35-fold magnification of the atomic cloud. The pixel size of the ProEM camera is $A = (0.455 \times 10^{-6}\, m)^2$. In the experimental setup objectives are placed above and below the glass cell both with a numerical aperture $NA = 0.5$ (solid angle of $\Omega = 0.13$).

Another important setup-dependent step is calculating the photon number and intensity from the counts recorded on the CCD. This calculation is necessary for determining the optical density (Eq. (2.14)) and the number of scattered photons per atom, N_{abs}.
The number of scattered photons is calculated from the actual count on the CCD without the atoms C_0 (reference image) and the count with the atoms C_1 (atom image). The number of scattered photons is given by:

$$N_{scatt} = -\mathcal{G}(C_0 - C_1) \tag{2.31}$$

where $\mathcal{G}$ is a factor accounting for (in order) the solid angle of the objective, the gain of the camera, the quantum efficiency of the camera and the reflection loss along the imaging path.

$$\mathcal{G} = 1.07 \cdot 0.89 \,/\, 0.8 \,/\, 0.77 \tag{2.32}$$

Those values are based on measurements performed on the imaging setup described in [2]. An actual intensity is calculated from the number of photons by using the energy of the photons $E_{ph} = \hbar\omega$, the size of the CCD-pixel A and the imaging pulse duration of the imaging laser t_{pulse}

$$I_j = \frac{N_j \hbar\omega}{t_{pulse} A}, \tag{2.33}$$

for $j \in 0, 1$. To calculate the number of absorbed photons per atom, the number of scattered photons per pixel is summed over the region of interest (ROI) and divided by the total number of atoms in the cloud:

$$N_{abs} = \frac{1}{N} \sum_{ROI} (N_0 - N_1) \tag{2.34}$$

When measurements are programmed in the experiment, the true intensity value is not used, instead a 'power factor' is used. To obtain a physically meaningful measure of intensity, the relationship between the power factor and the actual intensity incident on the atomic cloud was deduced.

Chapter 3

Local Calibration

The aim of this project was to obtain a better calibration of the absorption imaging used for the In-situ measurements of the density of the BEC. The previous calibration was done using a global calibration method described in section 2.3.1. The result of this previously used calibration is described in detail by Maurus Hans in [2] and [8], and considerations leading up to the calibration can be found in [15]. As discussed in section 2.3.1, the previously used calibration considered two effects as described by the formula:

$$od = \alpha \cdot ln\left(\frac{I_0}{I_1}\right) + \frac{I_0 - I_1}{I_{sat}}, \text{ with } \alpha = 7.3. \tag{3.1}$$

Considering the absorption of light by the atoms, and the effect of saturation. Here, I_0 is again the intensity of the reference image and I_1 the intensity of the atom image.

In this project the technique described in section 2.3.2 was used to obtain a more accurate calibration of the absorption imaging, taking into consideration, that the absorption behaviour of the atomic cloud can depend on the atomic density.

3.1 Effect of Multiple Scattering

Before the new calibration technique is discussed in detail, first a more intuitive understanding of the considered effect is given. The motivation of the new local calibration is to account for this density-dependent effect — which is necessary because the local density influences the local saturation intensity, making a global calibration inaccurate.

To study the impact, a higher local atom density has on the saturation of an atomic transition, images of the homogeneous atom cloud with several densities and imaging intensities are taken. In this way the change in the absorption of light with increasing intensity can be seen at different densities. As a measure of the absorptive capacity of the atoms, the scattered number of photons per atom N_{abs} is used. To minimize influences of the edge of the cloud, only a inner section of atom cloud was analysed. This makes the assumption of all atoms being in an area of approximately same density valid. To calculate this N_{abs}, the number of atoms in the ROI needs to be inferred for every density studied. In this analysis, the atom number was calculated using the final calibration result for homogenous clouds presented in section 3.5. As will be discussed later, this calibration has proven to keep the number of atoms in almost constant for

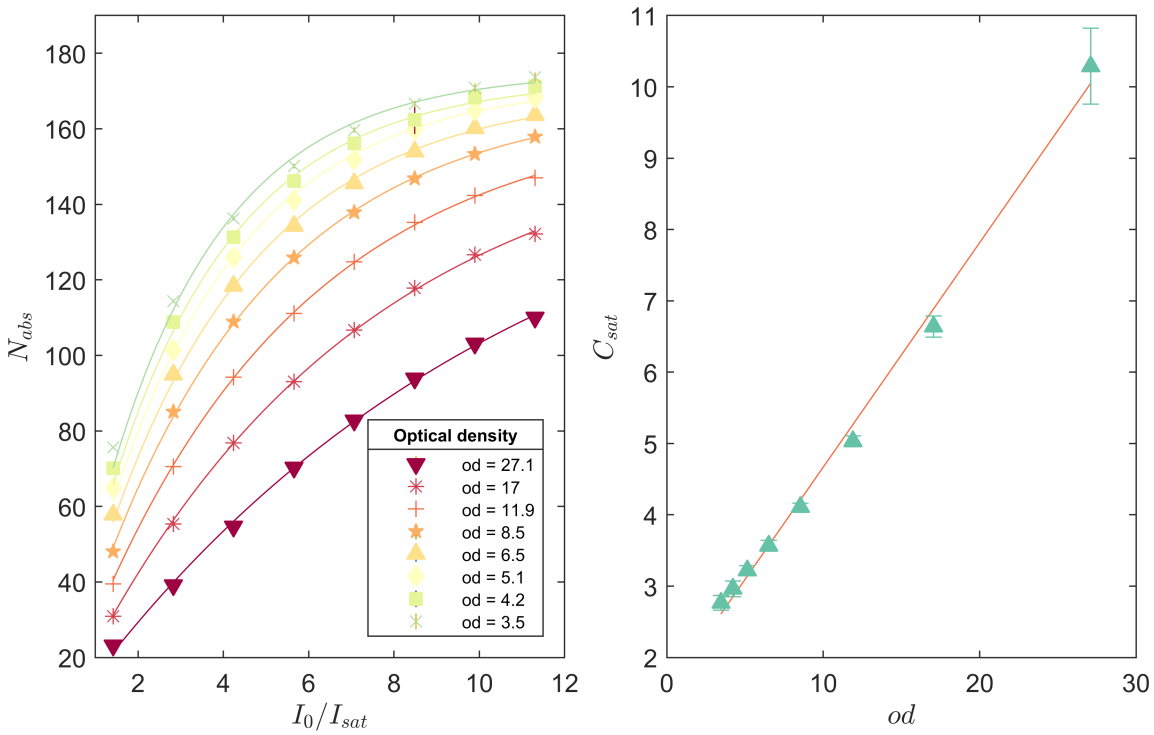

Figure 3.1: **Density dependent saturation of a homogenous atomic cloud imaged with** $11\mu s$**.** The left plot shows the behaviour of N_{abs} with increasing intensity for homogenous clouds of different densities (different colours/shapes). A fit of a saturation curve (Eq. (3.3)) is applied to the data and the results for the saturation parameter $C_{sat}(od)$ are shown on the right. The result of $C_{sat}(od)$ assures the assumption of a linear behaviour of $\alpha(od)$.

different imaging intensities and cloud sizes. To make the results presented in figure 3.1 even independent of any calibration, a constant total atom number of the cloud could be chosen, and the density could be calculated from the expansion of the measured cloud. The number of absorbed photons per atom N_{abs} are then calculated as described in section 2.34:

$$N_{abs} = \frac{1}{N_{atoms}} \sum_{ROI} (N_0 - N_1). \tag{3.2}$$

The results of $N_{abs}(od, I_0)$ are presented in figure 3.1 for a imaging pulse duration of $t_{pulse} = 11\mu s$. A clear increase of the scattered number of photons per atom is observed with decreasing density of the cloud. This points towards additional effects for higher densities leading to an earlier saturation of the atomic transitions. Therefore, only a smaller fraction of the imaging light can be absorbed. This difference in saturation is explained by multiple scattering of photons. Multiple scattering is expected to increase with the atom density, because a higher density increases the probability of absorption of an already scattered photon by surrounding atoms as explained in more detail in section 2.2.

To describe and compare the saturation observed for N_{abs}, a fit with the function

$$N_{abs} = N_0 \left(1 - \exp\left(-\frac{I_0}{C_{sat} \cdot I_{sat}}\right)\right), \tag{3.3}$$

is applied to the data. N_0 gives an estimation of the saturation limit of absorbed photons, I_{sat} normalizes the intensity to the theoretical saturation intensity of the transition and C_{sat} accounts for the change in the curvature of the saturation curve. This change of the saturation parameter $C_{sat}(od)$ is expected to follow a qualitatively similar trajectory as $\alpha(od)$, both accounting for the changing saturating behaviour of the atomic transition. The results of the fits are shown in figure 3.1 on right. A linear trend is apparent for $C_{sat}(od)$ justifying the later choice of a linear fit of $\alpha(od)$.

3.2 Local Calibration for Constant N_{abs}

To obtain a more precise calibration using the local calibration method presented in [3] a first measurement was taken of an atom cloud with a roughly radial symmetric Gaussian density profile to have regions of different densities. To calibrate the value of α different imaging intensities I_0 are needed. As previously described in section 2.3.2 the number of absorbed photons per atom N_{abs} is kept constant, as [3] proposes to reduce any effect a Doppler-Shift would have on the imaging, the imaging intensity and the pulse duration t_{pulse} are therefore varied. N_{abs} is expected to increase with higher intensities of the imaging beam as well as higher pulse durations, so short laser pulses are paired with high intensities and vice a versa to remain at a fixed value of N_{abs}. The behaviour was studied by a previous measurement and I_0 and t_{pulse} were chosen accordingly.

The methods described in the following sections were performed for each N_{abs} independently. The different parameter sets of t_{pulse} and I_0, each containing several pictures, were then averaged and those averages were used to calculate the value of α for a certain density region of the cloud.

3.2.1 Atom Cloud Regions of Constant Density

Two different methods were compared for identifying the regions of similar density. The first was the method presented by [3] using elliptical rings around the centre of the cloud. This method assumes radial symmetry of the cloud around the centre and an elliptical shape of the cloud. The elliptical shape of the cloud as well as the centre is found by performing a Gaussian fit to the profile of $I_0 - I_1$ in x- and y-direction. Masks of elliptical rings were then created as shown in figure 3.2.

The second method to identify regions of constant densities was finding masks based on the values of optical density per pixel obtained by the old calibration. A Gaussian filter was applied to the optical density of this reference picture to smooth out any minor fluctuations and the pixels were sorted in bins based on similar optical density. This method also leads to roughly radially symmetric masks, but better representing the actual shape of the density distribution of the atoms, as shown in figure 3.2.

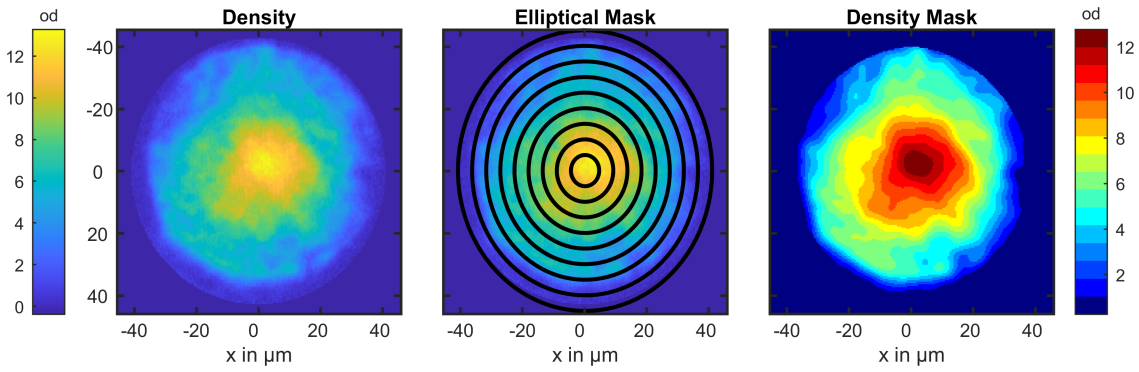

Figure 3.2: **Different masks for an absorption image.** The images presented are averaged over several pictures of an atomic cloud for an average number of absorbed photons per atom, $N_{abs} \approx 100$. The optical density calculated by the previously used global calibration is shown on the left. Regions of approximately constant optical densities needed for the local calibration are defined by two methods. Using elliptical masks following approximately the radial symmetric shape of the cloud (middle) and masks created based on the previously used density calculation (right). For the following evaluations, the method depicted on the right was used to determine regions of constant optical densities for the calibration.

The analysis to obtain $\alpha(od)$ was first done for both methods, but for the following analysis of the new measurements the second method was used, because this method produces regions of constant density more reliably.

3.2.2 Obtaining a Relation for $\alpha(od)$

After having identified the regions of similar od the local calibration method was used in each of the regions. This method is based on calibrations performed for cloud configurations at different values of N_{abs}. To set up measurements of constant N_{abs} another measurement was done before, studying the resulting N_{abs} for variations in t_{pulse} and I_0 and choosing the intensities for the following measurement accordingly. The value of α for each od-region is found by performing a linear fit of $\langle I_0 - I_1 \rangle_k$ over $\langle ln(I_0/I_1) \rangle_k$, using equation (2.14), and $\langle\,\rangle_k$ indicating the average values for all the pixel in the k-th region:

$$\langle I_0 - I_1 \rangle_k = \langle od \rangle_k - \alpha_k \left\langle ln\left(\frac{I_0}{I_1}\right) \right\rangle_k . \tag{3.4}$$

The slope of the fit gives a value for α_k, the intercept with the y-axis corresponds to the value of od_k in this particular region, as can be seen in figure 3.3. Each fitted curve in the figure corresponds to one region of optical density at different intensities, from small optical densities in the bottom left corner to high optical densities in the top right corner.

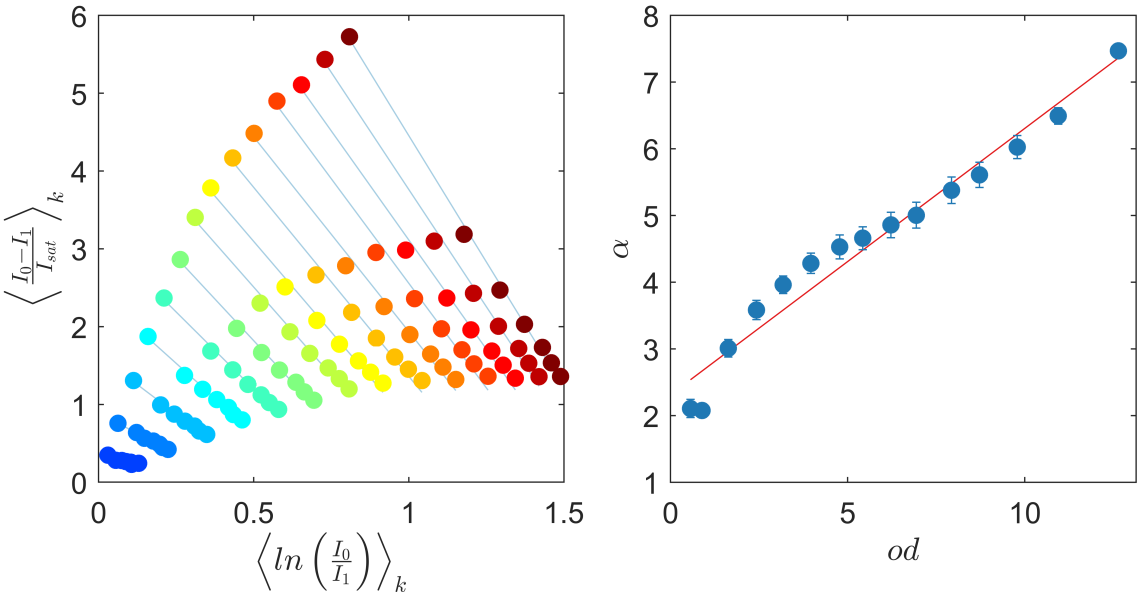

Figure 3.3: **Relation for $\alpha(od)$ for constant $N_{abs} \approx 100$.** On the left, $\langle I_0 - I_1 \rangle_k$ is plotted over $\langle ln(I_0/I_1) \rangle_k$ to obtain α and od according to equation 3.4. Each point corresponds to a set of pulse duration and imaging intensity ($I_0 \in ([1.4, 14] \cdot I_{sat})$, $t_{pulse} \in [7, 21]\mu s$) that together give $N_{abs} \approx 100$. For each set, ~ 20 pictures were averaged, and the analysis was performed on this mean picture. Each line corresponds to the k-th region of constant od. The slope of the linear fit (light blue) gives α_k, the intercept with the y-axis is od_k. On the right, the result of the fits $\alpha(od)$ (blue) are plotted with the assumed linear dependence (red). The deviation from the expected linear behaviour will be discussed later.

In a final step the result for α_k for every region is plotted over the corresponding value for the optical density od_k and a linear fit to the data is performed. The linear dependence of α on od is described by equation (2.18): $\alpha = \alpha' \cdot od + \alpha_0$.

In this way the relation for $\alpha(od)$ at $N_{abs} \approx 100$ turns out to be:

$$\alpha(od) = 0.43 \cdot od + 2.07.$$

This method was repeated for different values of N_{abs}, the results for $\alpha(od)$ for different N_{abs} are shown in figure 3.4.

The number of absorbed photons per atom N_{abs} is calculated for an atom number of $N \approx 75.000$, constant over different experimental realizations, and is calculated over the whole cloud following equation (2.31), which relies on the old, density-independent calibration. This calculation does not ensure a constant N_{abs} for each region of optical density, which will be further discussed in the context of the resulting calibration.

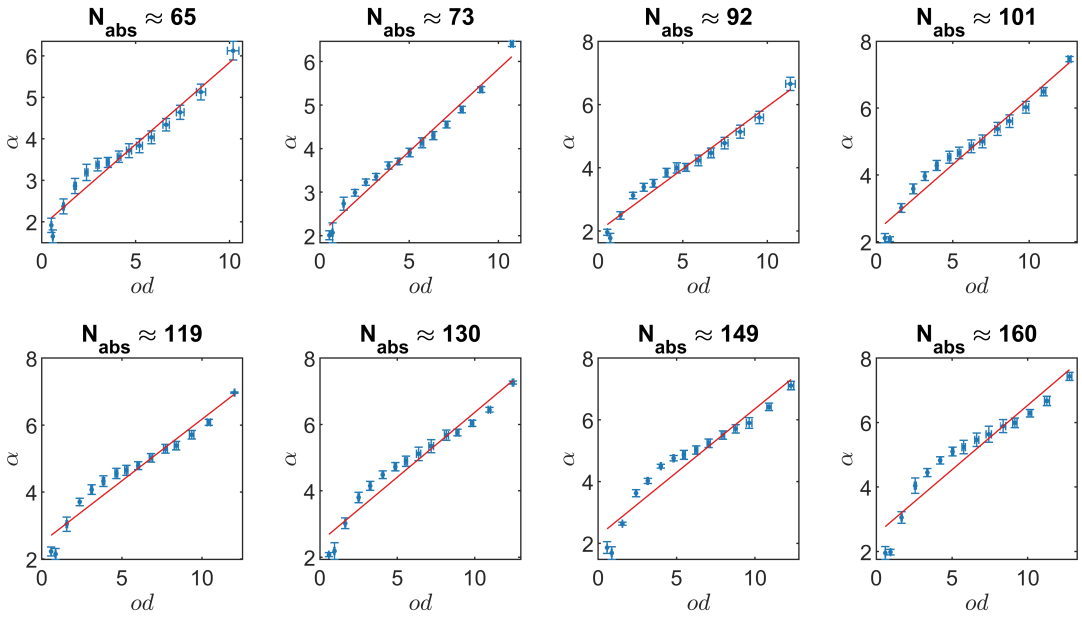

Figure 3.4: **Relation for $\alpha(od)$ for several number of scattered photons per atom** N_{abs}. Each plot depicts the relation of $\alpha(od)$ for one value of N_{abs} with an assumed linear relation. The deviations from this linear fit, will be discussed later. For each set, ~ 20 pictures were averaged, and the analysis was performed on this mean picture.

3.3 Results for Constant N_{abs} Calibration

To obtain a calibration for a number of scattered photons per atom N_{abs} the relation of $\alpha'(N_{abs})$ and $\alpha_0(N_{abs})$ was studied, the results are depicted in figure 3.5.

The final relation of $\alpha_0(N_{abs})$ and $\alpha'(N_{abs})$ is:

$$\begin{aligned} \alpha_0(N_{abs}) &= 0.0046 \cdot N_{abs} + 1.93 \\ \alpha'(N_{abs}) &= 0.0005 \cdot N_{abs} + 0.3. \end{aligned} \tag{3.5}$$

The results of the calibration show different trends. The general shape of $\alpha(od)$ is in good estimation a linear relation, the value of the fit at zero optical density should go to the theoretically expected value of the multi-level system (MLS) $\alpha = 2$ (see section 2.3.1). Values between $\alpha(od = 0) = 2$ and $\alpha(od = 0) = 2.8$ for different N_{abs} are observed. These results fit well with the expectation. The slope of $\alpha(od)$ is difficult to estimate theoretically and will be discussed later in the context of the new calibration results and in comparison to other calibration measurements and the 1D-model.

$\alpha_0(N_{abs})$ and $\alpha'(N_{abs})$ depict an increasing tendency, as also observed in [3], but especially the trend for $\alpha'(N_{abs})$ is not as obvious. To obtain a calibration for an arbitrary N_{abs} a linear relation was still assumed.

An interesting observation is the curved shape of $\alpha(od)$ for lower optical densities, a behaviour that can be observed for different values of N_{abs}. The reason for this behaviour is not yet clear and will be discussed in comparison to the 1D model in section 2.4. This

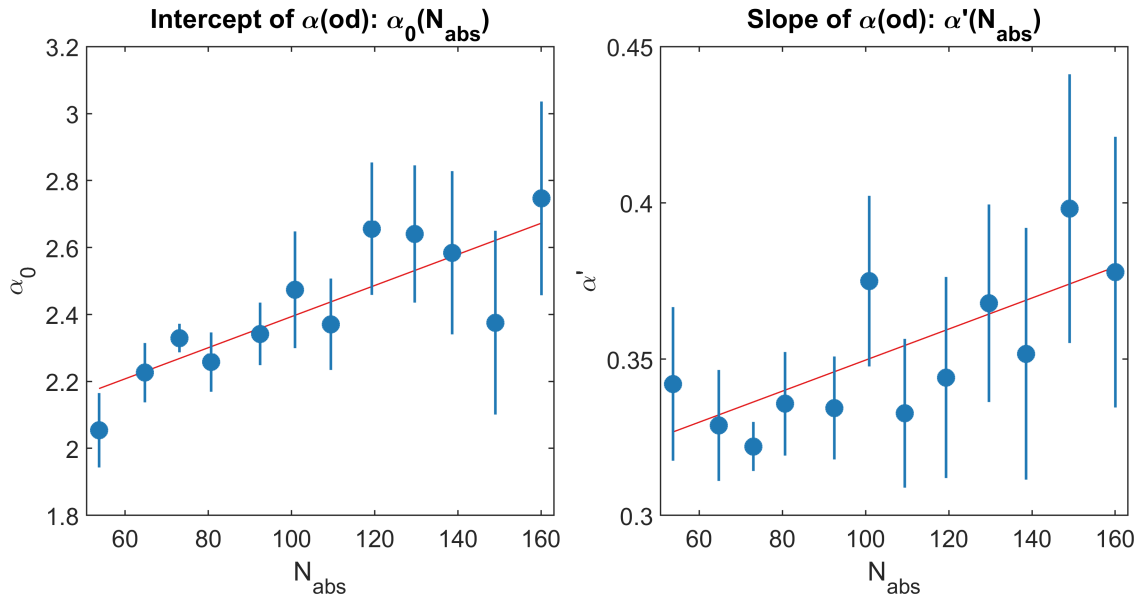

Figure 3.5: **Relation for $\alpha_0(N_{abs})$ and $\alpha'(N_{abs})$.** On the left the intercept of the linear fit of $\alpha(od)$ over od for different N_{abs}, on the right the slope of the linear fit of $\alpha(od)$ over od for different N_{abs}, extracted from the fits shown in figure 3.4. The assumed linear description (red) for both relations proposed in [3] is discussed below.

deviation from the linear model is highly relevant because the fit between the model for $\alpha(od)$ and the obtained trajectory greatly determines the quality of the calibration.

3.4 Calibration for Constant t_{pulse}

The original local calibration method by [3] keeps the number of absorbed photons per atom (N_{abs}) constant, trying to reduce the effect of the induced Doppler shift outlined in section 2.3.2. This builds on the method used by Reinaudi et al. [1] keeping the number of photons per laser pulse constant, by adjusting pulse duration in exchange for imaging intensity. During the analysis of the data the constant N_{abs} made the understanding of the results quite difficult, because too many different effects due to changes in intensity/pulse duration have to be considered. Also the N_{abs} mainly allow for a relative comparison between N_{abs}, because the *real* number of atoms cannot be inferred from the old calibration.
Because of this, the trajectory of $\alpha(od)$ is difficult to describe and thus not ideal to obtain a calibration. As an attempt to circumvent these uncertainties, the analysis was performed again, but this time the data was sorted by pulse duration t_{pulse}. Other than that, the same steps were performed as outlined in section 3.2. The calibration was now done solely considering changes in the imaging intensity and the following results were obtained.

As mentioned above, the problem with not paying attention to the number of absorbed photons per atom is that the results obtained for the optical density decrease with an increased number of scattered photons. Because the Doppler-shift induced by the scat-

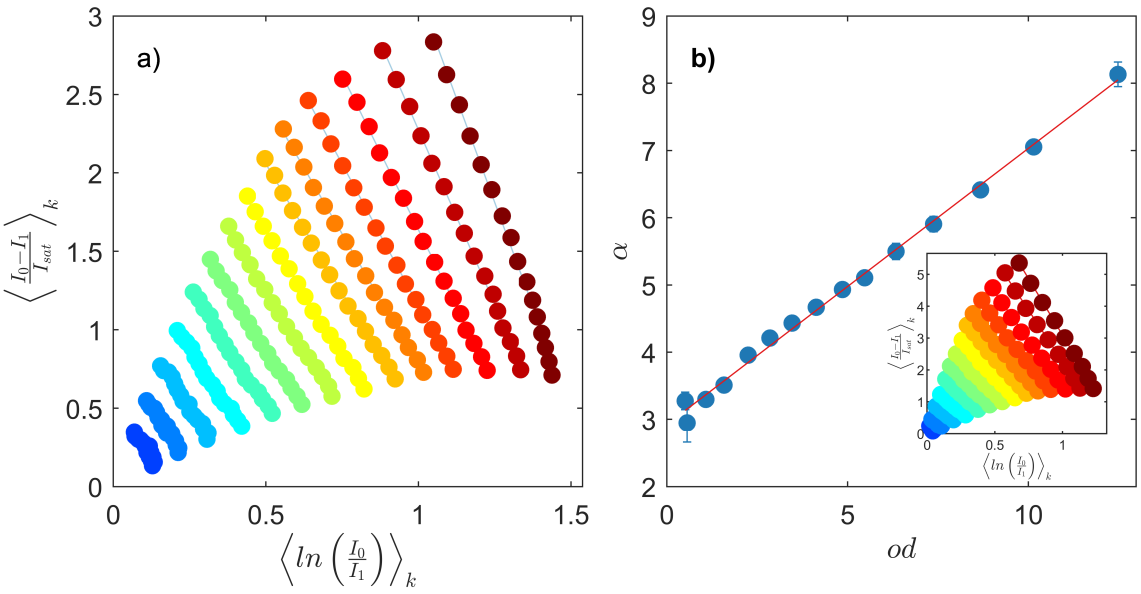

Figure 3.6: **Calculation of $\alpha(od)$ for $t_{pulse} = 17\mu s$ (left) and relation for $\alpha(od)$ at constant time $t_{pulse} = 11\mu s$ (right)**. On the left in part a) $\langle I_0 - I_1\rangle_k$ over $\langle ln(I_0/I_1)\rangle_k$ is plotted for $t_{pulse} = 17\mu s$ to show the deviation for high t_{pulse} from the linear relation. Each line corresponding to the k-th region of the cloud. On the right in b) this is also plotted for $t_{pulse} = 11\mu s$ in the inset and the main plot displays the result for $\alpha(od)$ with the assumed linear dependence. The data is taken for averaged images of ~ 20 single shots, at varying imaging intensity ($I_0 \in ([1.4, 14] \cdot I_{sat})$) and constant t_{pulse}.

tering of photons, shifts the resonance frequency which leads to a less efficient absorption of photons. This is then interpreted as a lower optical density.

The results obtained from this analysis with constant t_{pulse}, provide a clearer understanding of the processes to consider when calibrating an absorption imaging system. The relation between $\langle I_0 - I_1\rangle_k$ and $\langle ln(I_0/I_1)\rangle_k$ at different imaging intensities and optical densities show expected results for both high and low intensity limits. In figure 3.6 $\langle I_0 - I_1\rangle_k$ is again plotted over $\langle ln(I_0/I_1)\rangle_k$. Each fitted curve in the figure corresponds to one region of optical density at different intensities, from small optical densities in the bottom left corner to high optical densities in the top right corner. The low intensity limit corresponds to the data points at the right/lower side of the fitted curves; for those low intensities the logarithmic term of the optical densities dominates. The data points of the highest intensity correspond to the data points in the upper left corner of the fitted curve, here the linear term of the optical density dominates.
An interesting observation is the expected behaviour for high optical densities at low imaging intensities (see figure 3.6 a)) a deviation from the expected linear curve towards a pure domination of the logarithmic term is observed. This can be seen as the bend of the curves at high densities deviating from the obvious linear relation, towards a vertical trajectory.

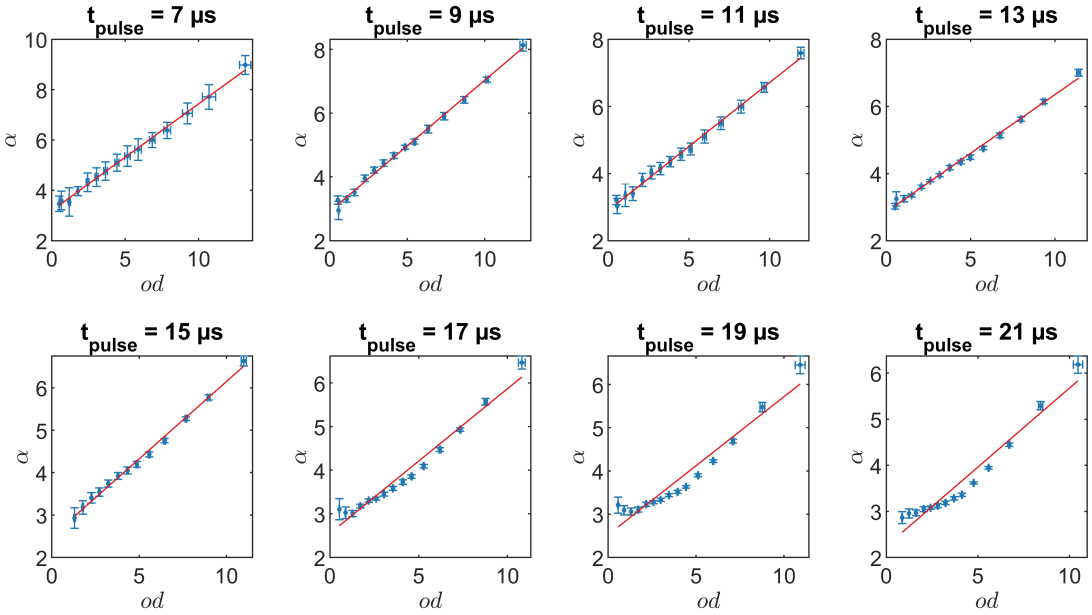

Figure 3.7: **Relation for $\alpha(od)$ at several pulse durations**. Each plot depicts the relation of $\alpha(od)$ for another imaging time t_{pulse} with a fitted linear relation. The data is taken for averaged images at varying imaging intensity ($I_0 \in ([1, 4, 14] \cdot I_{sat})$). For each set, ~ 20 pictures were averaged, and the analysis was performed on this mean picture.

This was again done for several different pulse durations and the results of the fits for $\alpha(od)$ are shown in figure 3.7. The relation of $\alpha(od)$ follows for small times a clearly linear relation, but for higher pulse durations the linear relation is not as clear.

The relation obtained for α at $t_{pulse} = 11\mu s$ is as follows: $\alpha(od) = 0.41 \cdot od + 2.92$.

In the final step again a more general calibration for constant pulse durations, characterized by α_0 and α' as in equation (2.18) was obtained. It is observed here that α_0 and α' decline linearly with increasing pulse duration. This is shown in figure 3.8 using all points as well as only the data points were the assumption of a linear dependence of $\alpha(t_{pulse})$ is valid around $t_{pulse} \approx 10\mu s$.

The final calibration of $\alpha(t_{pulse})$ is as follows:

$$\begin{aligned} \text{Using all points: } \alpha_0(t_{pulse}) &= -0.056 \cdot t_{pulse} + 3.55 \\ \alpha'(t_{pulse}) &= -0.008 \cdot t_{pulse} + 0.462 \\ \text{Fit around } 10\,\mu\text{s}: \alpha_0(t_{pulse}) &= -0.04 \cdot t_{pulse} + 3.33 \\ \alpha'(t_{pulse}) &= -0.013 \cdot t_{pulse} + 0.511 \end{aligned} \tag{3.6}$$

Again the results obtained for a calibration at constant imaging times t_{pulse} shall be evaluated in more detail. The general shape of the relation of $\alpha(od)$ is well described by a linear relation for times around $10\mu s$. For higher imaging times $\alpha(od)$ deviates from a linear curve by being flatter at lower optical densities and steeper at higher optical densities, see plots for $t_{pulse} \geq 17\mu s$ in figure 3.7.

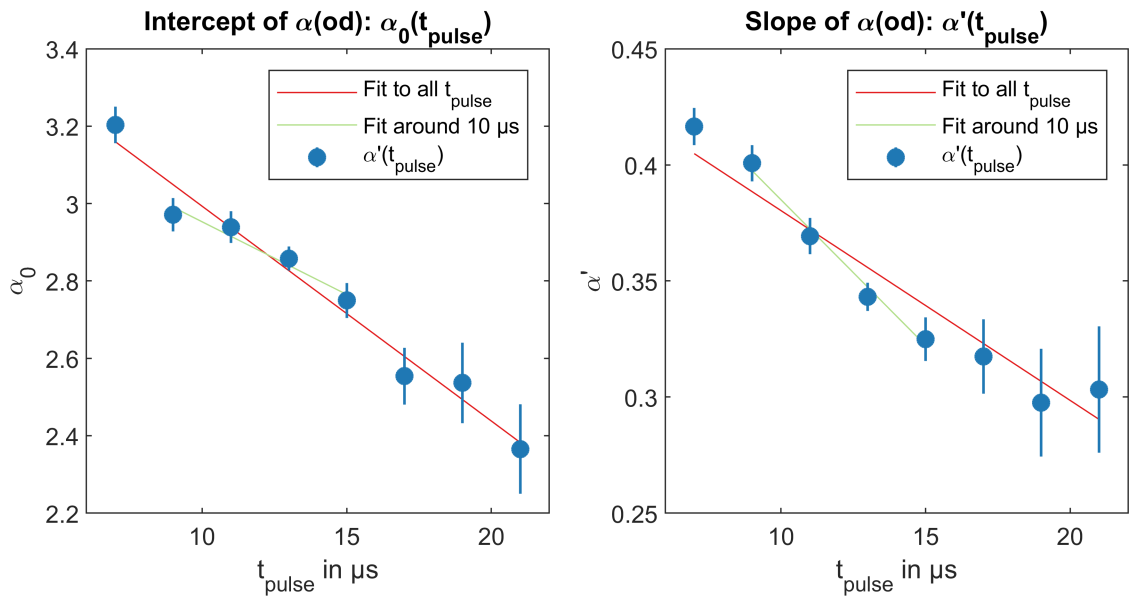

Figure 3.8: **Relation for $\alpha_0(t_{pulse})$ and $\alpha'(t_{pulse})$.** On the left the intercept α_0 of $\alpha(od)$ is depicted for different pulse durations, on the right the slope $\alpha^{'}$ of the linear fit of $\alpha(od)$ for different pulse durations is plotted. The linear fit to all data points is shown in **red**, the **green** line is the fit only described to the points around $t_{pulse} \approx 10\mu s$, where the behaviour of $\alpha(od)$ is best described linearly (see fig. 3.7). The obtained relations are used as an calibration for arbitrary t_{pulse}.

The theoretically predicted value of α at zero optical density is again $\alpha(od = 0) = 2$, based on the multi-level system used for the imaging. The value decreases approximately linear for higher pulse durations from around $\alpha(od = 0) \approx 3.2$ to $\alpha(od = 0) \approx 2.4$. This decline with higher imaging pulse durations would correspond to an increasing value of the effective cross section of the atoms σ_0^{eff}, which can be understood as more intensity needed to further saturate the transition. In other words less saturation at comparable intensity and surrounding density is expected for higher imaging times. This could be due to the influence of the Doppler shift at higher pulse durations explained below in more detail.

Those observations question which analysis to use for the final calibration. In section 3.6 a more detailed discussion of which calibration to choose will be provided based on the stability of the atom number for different cloud sizes/different intensities for the two calibrations.

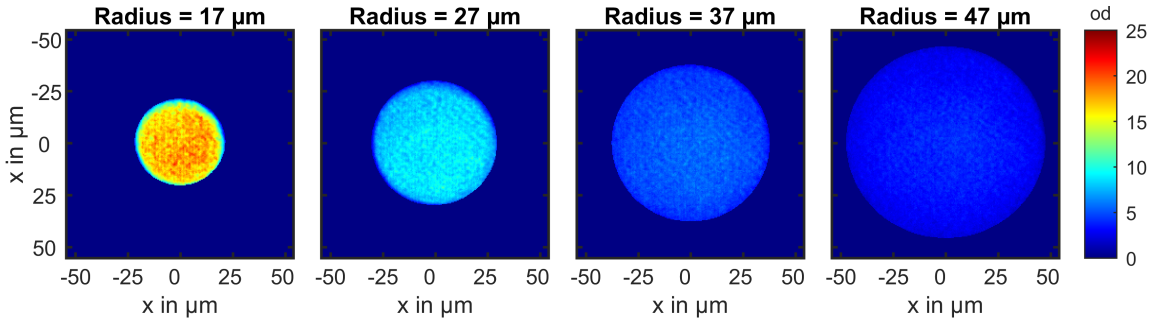

Figure 3.9: **Different sizes of clouds with homogenous density distribution.** The new local calibration was also performed based on clouds with different cloud sizes, but approximately constant numbers of atoms, to study different densities. This approach minimizes the influence of effects due to a density gradient in the atomic cloud by using a homogenous density distribution across the cloud. The images are mean images of ~ 20 single shots, and the optical density is already calculated using the new local calibration.

3.5 Homogenous Cloud

During the analysis the question arose as to whether the density profile of the clouds has an influence on the calibration of α. Under the assumption of multiple scattering the density of the atoms in the neighbouring region should have an influence on the change of I_{sat}^{eff}. Especially at the edges of the cloud this will have an effect, because fewer atoms contribute to the background of scattered photons.

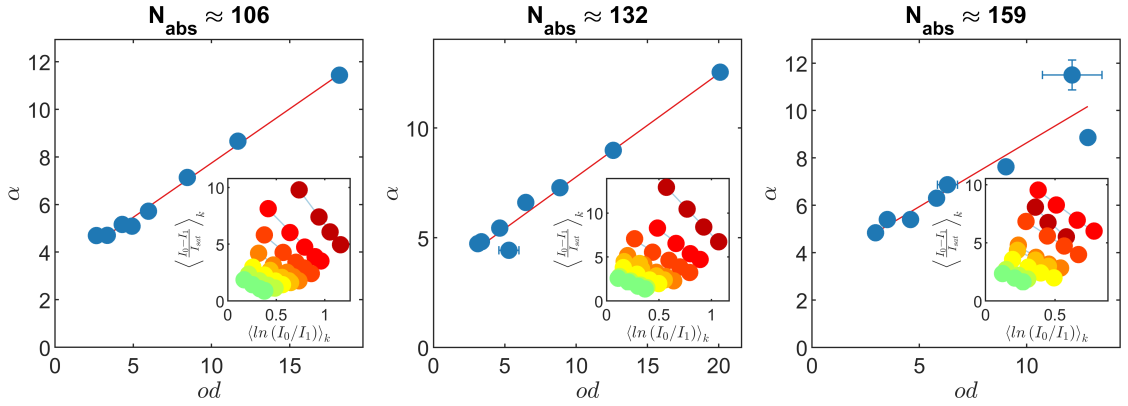

Figure 3.10: **Relation for $\alpha(od)$ for homogenous clouds for different N_{abs}.** The data is taken for averaged images at varying imaging intensity and pulse durations ($I_0 \in ([1.4, 14] \cdot I_{sat})$, $t_{pulse} \in [7, 19]\mu s$) to achieve constant N_{abs}. This measurement needs to be understood more qualitatively, because only ~ 5 single atom images are averaged per mean image. This was repeated for different cloud sizes from 17 to $50\mu m$. The inset shows $\langle I_0 - I_1 \rangle_k$ over $\langle ln(I_0/I_1) \rangle_k$ for the different cloud sizes/optical densities.

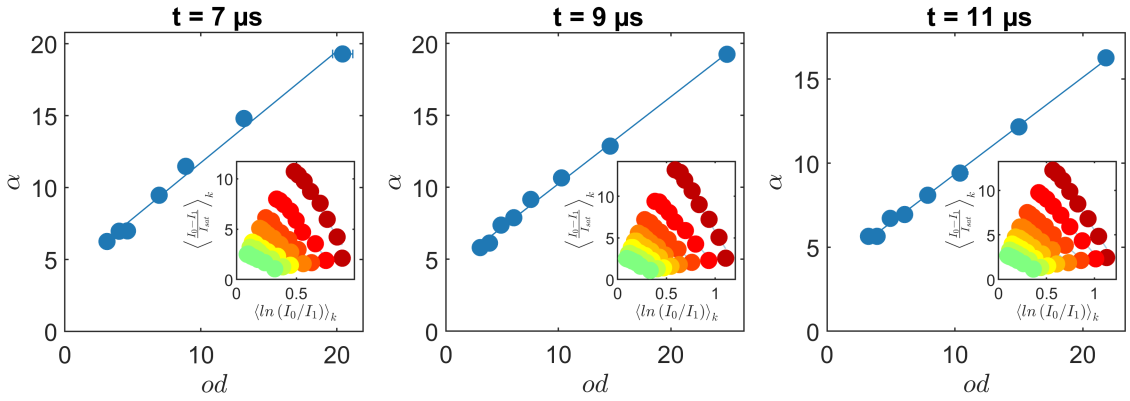

Figure 3.11: **Relation for $\alpha(od)$ for homogenous clouds for different pulse durations t_{pulse}.** The data is taken for averaged images at varying imaging intensity ($I_0 \in ([1.4, 14] \cdot I_{sat})$) at constant imaging time t_{pulse}. This was repeated for different cloud sizes from 17 to 50μm. In the inset, $\langle I_0 - I_1 \rangle_k$ over $\langle ln(I_0/I_1) \rangle_k$ is shown for the different cloud sizes corresponding to the different optical densities used for the calibration. The measurements at $t_{pulse} = 7\,\mu s$ and $t_{pulse} = 9\,\mu s$ need to be understood more qualitatively, because only ~ 5 single atom images are averaged per mean image. The measurement at $t_{pulse} = 11\,\mu s$ is based on 24 averaged single shots, and thus provides more reliable quantitative results.

To examine this question in more detail, another measurement was performed using clouds with a homogeneous density profile in the x-/y-plane and an approximately constant number of atoms in the cloud (realized by the same loading scheme for all clouds). To perform measurements at different densities different cloud sizes were realized, leading to different optical densities, this is shown in figure 3.9. The loading scheme is programmed to expand the cloud, and therefore the number of atoms could only decrease by losing atoms, but never increase for bigger clouds. The calibration was obtained again using the method described above for determining α from different intensities and masking the cloud cutting of the edges, to neglect effects of less MS at the edges.

The calibration was again performed for a constant number of absorbed photons N_{abs} and constant imaging pulse duration t_{pulse}. The results of this calibration are shown in figures 3.10 and 3.11.

The results show qualitatively the same linear trend as observed in measurements performed for clouds with a linear density profile. The values for $od = 0$ are also in a comparable range at around $\alpha(od) \approx 3$, also the incline of the linear fit is comparable for similar t_{pulse}/N_{abs} in clouds with a linear density profile. The exact comparison is presented in figure 3.12. The linear fit seems to describe the calculated values for the homogenous cloud even better. This could also be due to a smaller sample size of different od's which makes it difficult to observe non-linear trends.

In figure 3.12 the obtained calibrations from a homogenous density and a linear density profile for $N_{abs} \approx 100$ and $t_{pulse} = 11\mu s$ are plotted together. Systematically higher

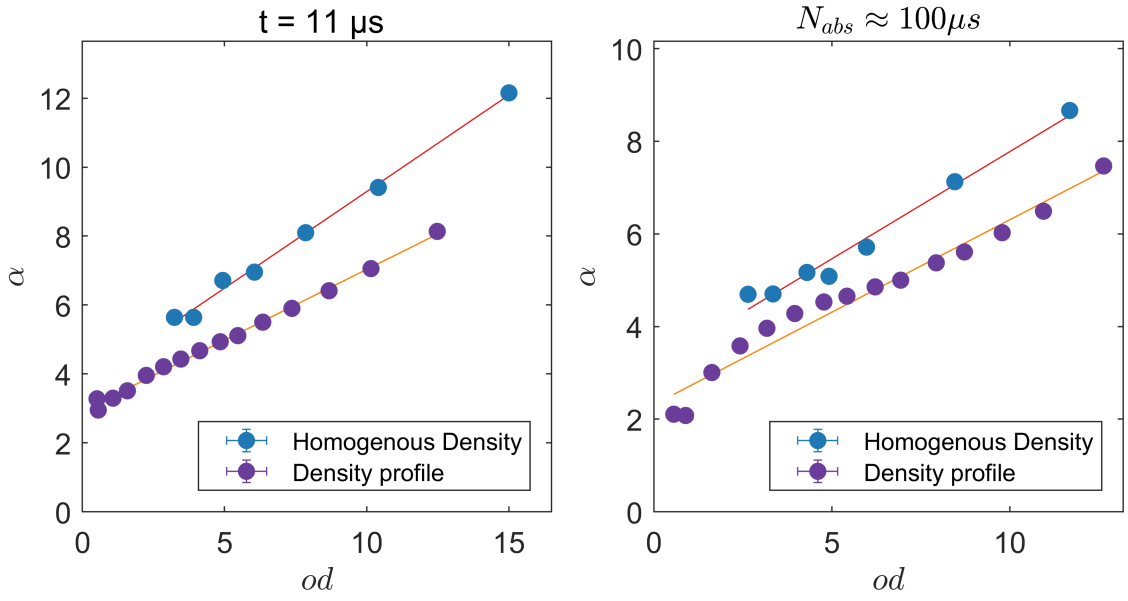

Figure 3.12: **Relation for $\alpha(od)$ based on a homogenous density (blue/red) and based on clouds with a linear density profile (purple/orange) for a pulse duration of $t_{pulse} = 11\mu s$ on the left and $N_{abs} \approx 100$ on the right.** The errors bars are smaller than the markers used and therefore not visible. A systematic higher value of $\alpha(od)$ for the homogenous clouds can be observed in comparison to the calibration based on clouds with a linear density profile. This demands to take the density distribution in the atom cloud into account when considering multiple scattering effects.

values of $\alpha(od)$ for the homogenous cloud can be observed. The calibration based on the homogenous clouds shows a higher incline of $\alpha(od)$ and therefore the two different calibrations are similar at low optical densities but deviate largely at higher optical densities. This can be explained in the multiple scattering picture taking into consideration the density of the surrounding atoms. In the homogenous cloud by design only one spatially flat density of atoms is produced (neglecting effects of the edges), while in the case of the linear density profile the higher optical densities are always surrounded by regions of lower densities. Therefore less multiple scattered photons from neighbouring regions are expected to additionally saturate the atoms in high density regions in the case of a linear density profile.
Thus, for the same optical density, more multiple scattered photons from neighbouring atoms are present in the case of homogeneous clouds, leading to a higher value of α.

This observation raises questions about the validity of the calibration for different density profiles possibly realized in the experiment. In the following sections the produced calibrations will be applied to different data sets to evaluate the consistency of the atom number for different cloud sizes and different imaging intensities.

3.6 Results of Local Calibration

The calibration is obtained as described in the previous section for constant N_{abs} and constant t_{pulse}. Both calibrations are applied to the data sets used for the calibration and the results for different imaging intensities are compared to the previous calibration. In a second step, the calibrations were applied to data sets with varying cloud size and, therefore, different atomic densities at approximately constant atom number. With the previous calibration more atoms were measured for a more dilute cloud, while the total atom number is assumed to be constant. This observation is expected because the atoms are less saturated by the surrounding light field of the rescattered atoms. The new calibration shows a more constant measured atom number for different cloud sizes, because the calibration is done considering density-dependent scattering effects.

3.6.1 Atom Number for Different Intensities

The first test for the general calibrations $\alpha(N_{abs}, od)$ and $\alpha(t_{pulse}, od)$ obtained from the clouds with a linear density profile was done by applying them to the clouds the calibration was based on and studying the behaviour of the atom number deduced for varying intensity. In figure 3.13, this was done for a measurement with same t_{pulse} at different intensities (green). In orange the results for the same data sets using the old calibration are shown. This is similarly done in figure 3.14 for data sets with comparable N_{abs} and varying intensity.

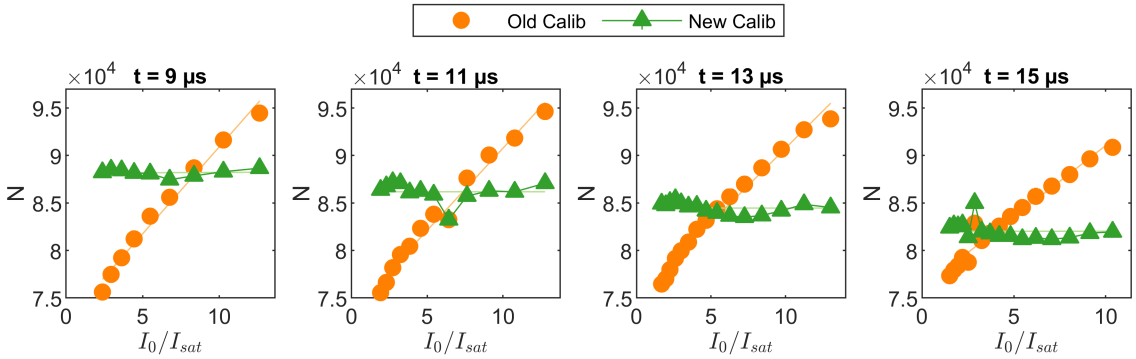

Figure 3.13: **Calibration based on linear density profile and constant t_{pulse} applied at different intensities for several different pulse durations**. The **orange** data points show the atom number calculated from the optical density using the old global calibration. The **green** data points show the atom number calculated from the optical density using the new local calibration based on the linear density profile. The atom number calculated from the new calibration is significantly more constant across different densities and pulse durations. Error bars are plotted for the new local calibration, but the markers are bigger than the error bars.

In figure 3.13 the results of the new calibration (green) show a more consistent number of atoms calculated from the optical density for different imaging intensities in comparison to the atom number based on the old calibration (orange). In comparison to the results of the new calibration the old calibration underestimates the number of atoms at

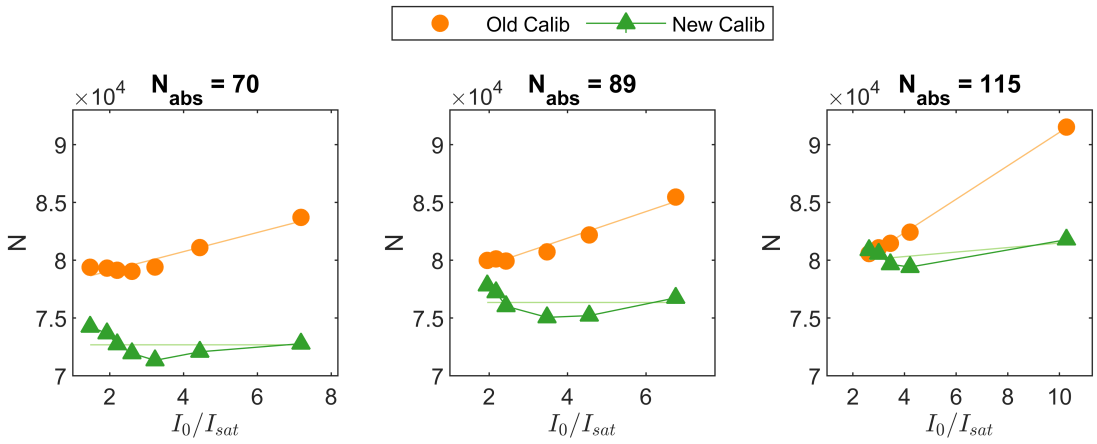

Figure 3.14: **Calibration based on linear density profile and approximately constant** N_{abs}. The **orange** data points show the atom number calculated from the optical density using the old global calibration. The **green** data points show the atom number calculated from the optical density using the new local calibration based on the linear density profile. The atom number calculated from the new calibration is significantly more constant across different densities and N_{abs}'s. Error bars are plotted for the new local calibration, but the markers are bigger than the error bars.

lower intensities and overestimates them at high intensities. At constant t_{pulse}, the old calibration shows a deviation of up to $\sim$ 20.000 atoms in between different intensities. Independent of the new calibration, the atom number is expected to be approximately constant, because the same loading scheme is used and for every picture several shots are averaged. The huge difference in the atom number by the old calibration is probably due to the fact that during the old calibration, the global calibration method was used for one specific setup of imaging pulse duration and density profile of the cloud. The old global calibration of $\alpha = 7.3$ is therefore exactly precise only for one certain average atomic density and cloud configuration.

As can be seen the new calibration based on the pulse duration provides a consistent atom number for different pulse durations. The comparison between different pulse durations shows a trend towards a lower atom number for higher pulse durations. This increase in the mean atom number could be due to the induced Doppler shift, leading to a less efficient absorption of the atoms and therefore a lower optical density is assumed.

The same test is done for the new calibration based on the constant number of absorbed photons per atom. The results are shown in figure 3.14. The new calibration based on constant N_{abs} provides a more constant atom number for different intensities, but the results seem to be not as reliable as the calibration based on pulse duration. For the case of constant N_{abs} the old calibration also seems to produce a more consistent atom number for different intensities than considering the case of constant t_{pulse}. For higher intensities and N_{abs} the inconsistency of the old calibration becomes more obvious. Even though the results for the new calibration based on constant N_{abs} are not as consistent as those based on the calibration with constant t_{pulse}. Interestingly an increase of the new measured total atom number is observed with increasing number of absorbed atoms.

3.6.2 Atom Number at Different Cloud Sizes

The biggest challenges motivating the new calibration, arose during measurements of different cloud sizes, which led to a significant increase in atom number with the size of the cloud (corresponding to a lower density at assumed constant atom number). This is again due to the underestimation of high densities by not accounting for multiple scattering effects. To tackle this challenge, a measurement was done with a preserved atom number, but varying density by modifying the expansion of the cloud. When letting the atom cloud expand further it is only ever expect to lose atoms, but never to gain atoms, as was observed with the old calibration. Therefore, this measurement is perfect to test the improvements made with the new calibration.

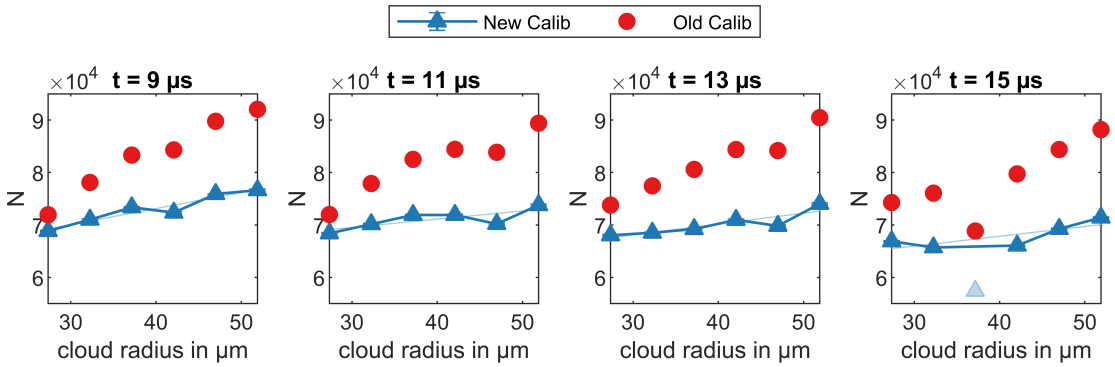

Figure 3.15: **Calibration based on linear density profile at constant t_{pulse} applied to different cloud sizes**. This figure shows the calculated total atom number for a circular shaped density with various radii for the old and new calibration method (red/blue). The clouds have a homogenous density profile and smaller cloud sizes corresponds to higher atomic densities (visualized in fig. 3.9). The **blue** data points show the atom number calculated with the new calibrations, the **red** data points show the atom number calculated with the old calibration. Only densities were compared, where the new calibration was also calibrated for. Error bars are plotted for the new local calibration, but the markers are bigger than the error bars. For $t_{pulse} = 15\,\mu s$ the transparent data point is excluded from the fit. Significant improvements in the consistency of the atom number can be observed.

In figure 3.15 the results of the new calibration based on the linear density profile and constant t_{pulse} are shown for different cloud sizes. The clouds have a homogenous density profile, thus deviations are expected applying the calibration based on the linear density profile. In comparison to the old calibration, the new calibration shows a clearly more constant atom number at different cloud sizes for the same imaging intensity. The old calibration shows a trend towards a higher atom number for bigger cloud sizes, which is expected due to the underestimation of the optical density for higher densities. This observation is expected in the context of multiple scattering as described in section 2.2. The new atom number based on the calibration using a linear profile deviates not much between different pulse durations. For this comparison it is important to say, that only densities were used which were also comparably realized in clouds with a linear density profile and a reliable calibration existed for those densities.

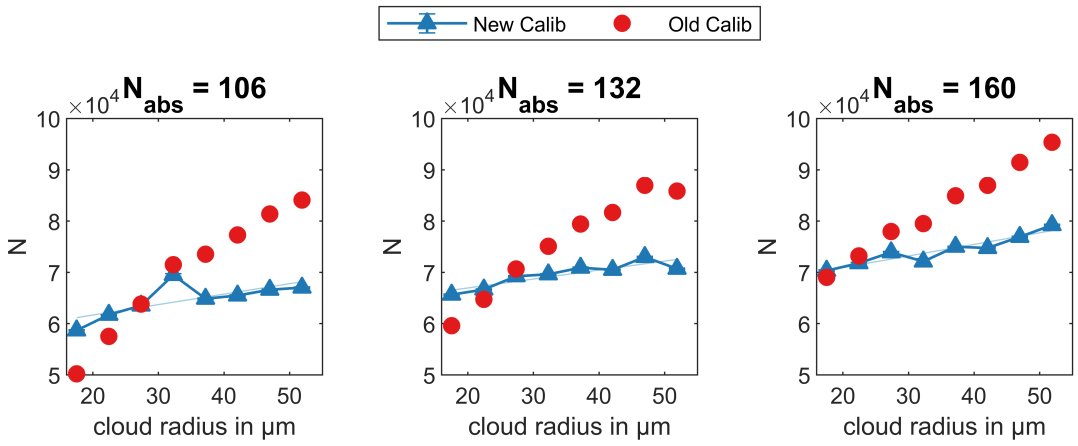

Figure 3.16: **Calibration based on constant N_{abs} and linear density profile applied to different cloud sizes**. For three different number of absorbed photons per atom N_{abs} the results of the new calibration based on the linear density profile are applied to a circular shaped density with various radii for the old and new calibration method (red/blue). The clouds have a homogenous density profile and lower cloud sizes corresponds to higher atomic densities. The **blue** data points show the atom number calculated with the new calibrations, the **red** data points show the atom number calculated with the old calibration. Significant improvements in the consistency of the atom number can be observed. The markers are bigger than the error bars of the new calibration.

This comparison was again also done for the calibration based on constant N_{abs}, the results are shown in figure 3.16. Also, the results show a more consistent atom number across different cloud sizes (densities) for the new calibration based on constant N_{abs} in comparison to the old calibration. The old calibration shows a trend towards a lower atom number for smaller cloud sizes, which is expected due to the underestimation of the optical density for higher atomic densities. Unfortunately, again a trend is observed where the mean total atom number based on the new calibration increases with increasing numbers of absorbed photons. This is an interesting observation, but does not question the improvement of the new calibration.

In a final step, the calibration based on the linear density profile and the homogenous density profile were compared for different cloud sizes (densities) of homogenous clouds, a more consistent atom number is expected from the calibration based on the homogenous clouds, because they were calibrated for exactly this case. Both calibrations are compared for constant t_{pulse} and constant N_{abs} each applied to one example in figure 3.17. The results show a more consistent atom number for both calibrations in between different cloud sizes.

It can be seen in figure 3.17, that the linear density calibration fails to account for a clear underestimation of the number of atoms at densities beyond the densities used for the calibration. This is expected, but if the relation of $\alpha(od)$ were in good approximation linear, the atom number should not deviate as much as it does. It could also be that the linear density profile fails to correctly quantify the influence the multiple scattering has. One reason for this could be the fundamental difference of the influence of neighbouring

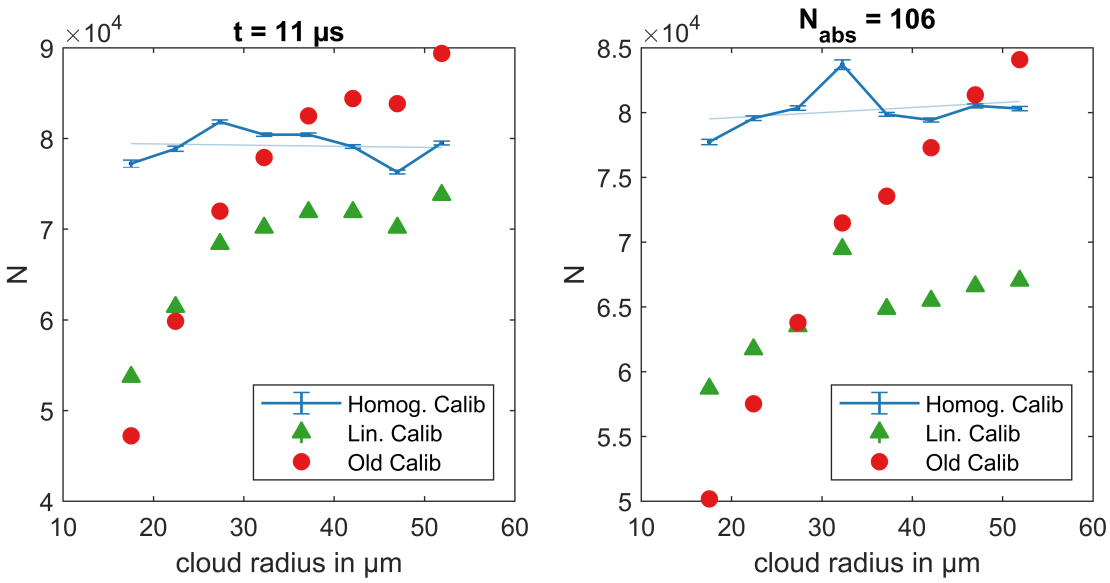

Figure 3.17: **Comparison of calibrations based on different density profiles applied to varying cloud sizes**. In the left plot, the calibration for constant t_{pulse} based on a homogenous and linear density profile is applied to different cloud sizes. In the right plot, the calibration for constant N_{abs} based on a homogenous and linear density profile is applied to different cloud sizes. In both plots, the **red** values are calculated using the old calibration, the **green** triangles are calculated from the new calibration based on the linear density profile, and the **blue** dots are calculated from the new calibration based on the homogenous density profile. It can be seen that the calibration based on the homogenous density profile provides a more consistent atom number across all different cloud sizes/densities. The calibration based on the linear profile only performs significantly better than the old calibration for the density, also considered in the calibration. The error bars for the new calibrations are partly smaller than the marker size.

regions depending on the density distribution. In the linear density case the neighbouring regions of high density regions contribute less to the multiple scattering, because they are at lower density. While for the homogenous case the whole cloud is at a higher density, therefore neighbouring regions contribute more re-scattered photons. This could explain why the calibration based on a linear density profile underestimates the optical density. But in between both measurements, changes to the experimental setup were made, which could relate to a different amount of atoms in the cloud influencing the conclusions drawn from the calibration.

The atom number calculated with the old calibration varies from $N \approx 47.000$ at highest density to $N \approx 90.000$ at lowest densities, for the example at $t_{pulse} = 11\mu s$. When either new calibration method is used in the regime it was calibrated for the atom number is rather constant, with the calibration using homogenous clouds of course being more consistent when again applied to homogenous clouds.
These results raise the question whether the density distribution of the cloud has a considerable influence, through collective multiple scattering effects, and should also be considered in future calibrations.

3.7 Single Pixel Analysis

Another attempt was made to further verify the relation of $\alpha(od)$ to be approximately linear. A method presented in [7] was used to combine the idea of the Global Calibration method (which minimizes the fluctuations of the *od* over different intensities) with a spatially resolved approach, by performing this minimization pixel by pixel. To account for small shifts due to noise of the atom distribution, the centre of gravity of the cloud for each picture is aligned. Because the validity of this assumption is questioned, this method is only used to provide another indication of the general trend of $\alpha(od)$ instead of a precise calibration.

In figure 3.18 the results of the single pixel analysis are shown for different atomic densities at a constant $t_{pulse} \approx 11\,\mu s$ for atom clouds with a homogenous profile. For each pixel, α is varied to minimize the variation of *od* at different imaging intensities, as shown in the inset for one pixel. In the main figure, the value of α over *od* for every pixel is plotted. This is done for eight different cloud sizes, each corresponding to a different atom density. A linear fit is applied to all data points plotted to calculate the mean expected α for every *od*.

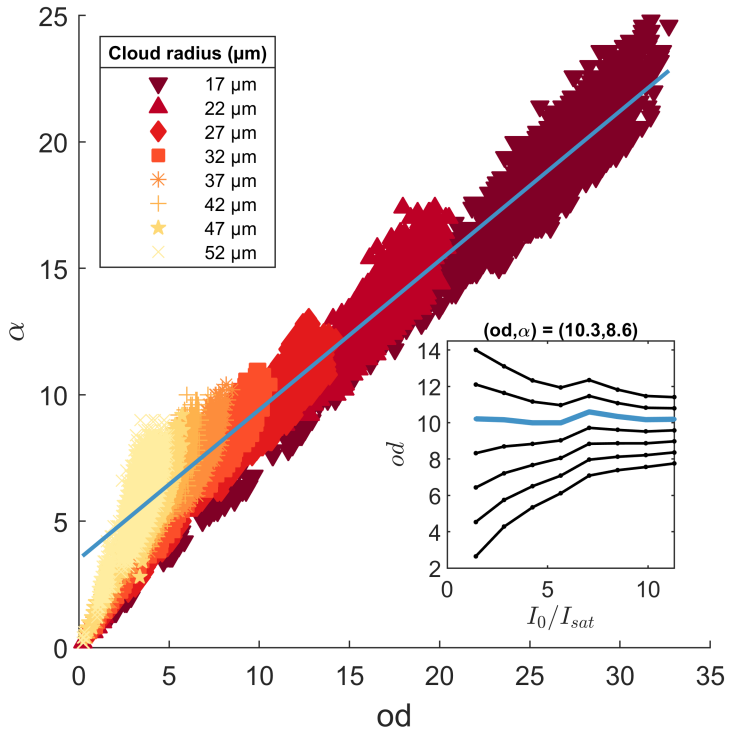

Figure 3.18: **Estimation of $\alpha(od)$ through pixel-by-pixel alpha variation**. The different symbols with different colors correspond to different cloud sizes and respectively different densities, all imaged at constant pulse duration $t_{pulse} = 11\,\mu s$. Each point represents (od,α) for one pixel, calculated by minimizing the deviation of *od* vs. I_0, as shown in the inset. To all those points a linear fit is performed resulting in the following relation: $\alpha = 0.59 \cdot od + 3.50$. Figure inspired by [4].

The results confirm a linear dependence of $\alpha(od)$. The intercept of the fit corresponds to the behaviour assuming no neighbouring atoms, and therefore, does only account for multiple scattering effects between the atoms of one pixel. The intercept calculated from the fit is in good agreement with the values obtained from the other calibration methods at around $\alpha(od = 0) = 2.82$. This value also agrees with the theoretical expectation of $\alpha > 2$ with the theoretical value of the specific closed optical cycle used as a lower bound.

3.8 Signal to Noise

One of the criteria for choosing parameters for the intensity and imaging durations of absorption imaging is a good signal-to-noise ratio. The value of t_{pulse} highly depends on the required spatial resolution, because atoms should not move by more than one pixel during the imaging pulse, therefore with shorter imaging times a higher resolution is achieved. The measurements in the experimental setup are also limited to pulse durations above $2\mu s$ because only after this time is a similar population achieved for both transitions used in the multi-level system. This section, therefore, determines the signal to noise ratio at different laser intensities for measurements around $10\mu s$.

A maximum in the signal-to-noise-ratio is expected at a certain intensity of the imaging laser. The noise due to fluctuations in the amount of photons, detected on the CCD camera, behaves as

$$\sigma_S \propto \sqrt{N_{ph}}, \tag{3.7}$$

with N_{ph} being the number of photons, and where only the noise of the laser itself is considered. The number of photons increases linearly with the imaging intensity.

As a measure for the signal the calculated number of atoms in the cloud N_{atoms} is used, which is determined from the optical density for every pixel with the new calibration. To obtain a measure for the noise related to the signal of interest, the standard deviation of the optical density is calculated for an area far away from the cloud which contains no atoms and therefore all fluctuations between pixels should be due to noise on the camera.

The results of the signal and noise for different imaging intensities and different pulse durations can be found in figure 3.19. A clear minimum of the noise at a power of around $4\, I_{sat}$ is observed which corresponds to an actual intensity of the imaging laser of $I_0 \approx 7.0 \frac{mW}{cm^2}$. This minimum is explained by an almost constant number of atoms in the cloud and an increase in the noise of the camera with increasing intensity. Because the noise of the imaging laser scales as $\sigma_S = \Delta I_0 \propto \sqrt{I_0}$, when the noise of the optical density is calculated outside the atomic cloud with equation (2.14), the intensities I_0 and I_1 should be equal except for the random noise on both intensities. The noise of the optical density is then calculated from equation (2.14) using error propagation as

$$\Delta od = \sqrt{2\left(\left(\frac{\alpha}{I_0} + 1\right)\Delta I_0\right)^2} = \sqrt{2\left(\frac{\alpha}{\sqrt{I_0}} + \sqrt{I_0}\right)^2}. \tag{3.8}$$

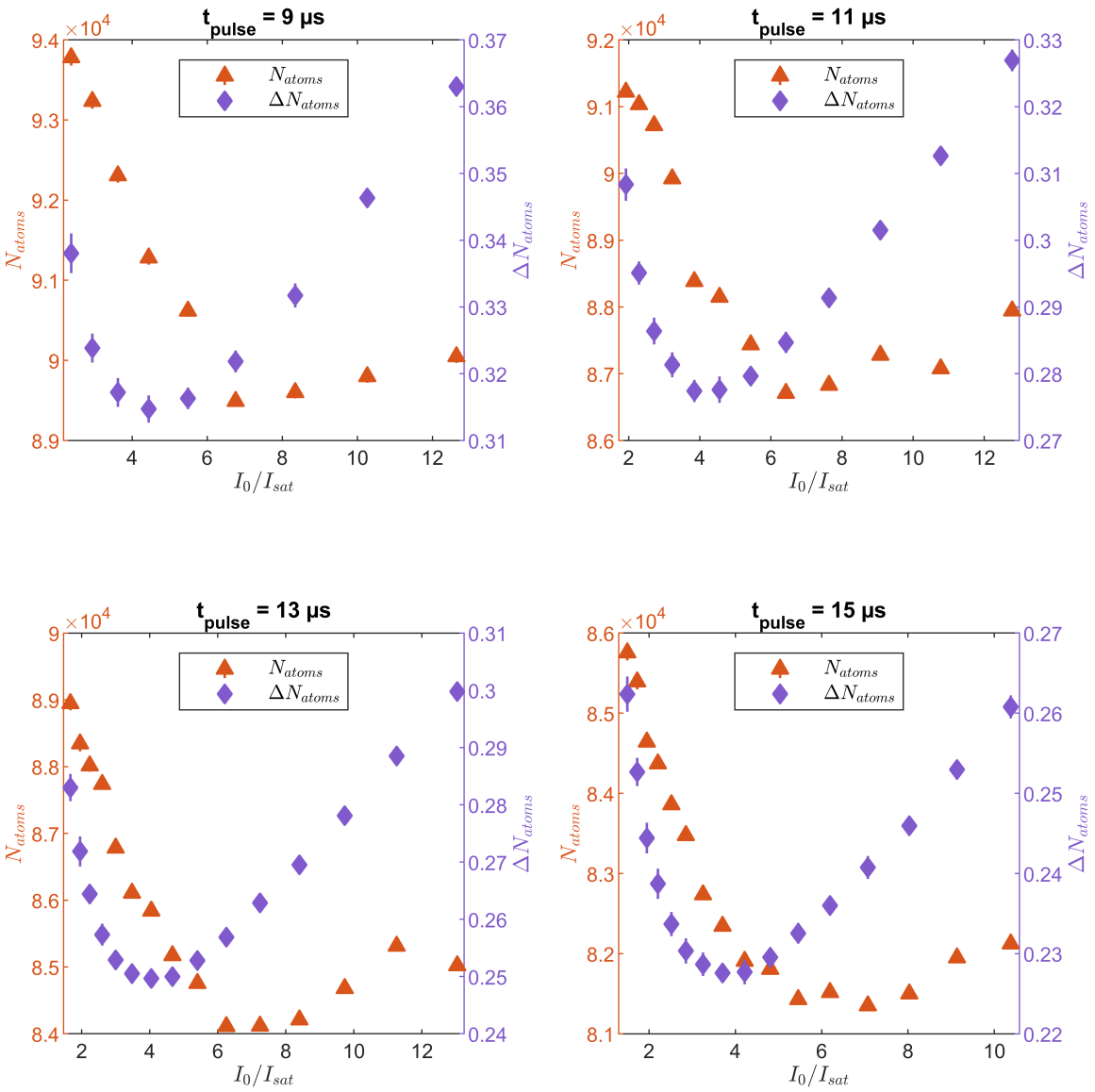

Figure 3.19: **Signal-to-Noise at different imaging times and intensities**. The number of atoms N_{atoms} (red), calculated for every single image individually, is calculated with the new calibration based on constant t_{pulse} and is compared to the noise of the laser ΔN_{atoms} (blue) calculated as described above. A minimum of the noise is observed at small intensities around $4\,I_{sat}$ for all pulse durations.

For the calibrated value of alpha close to zero optical density of $\alpha \approx 2$, this describes the relation of $\Delta od(I_0)$ reasonably well. The figure shows the atom number N_{atoms} as well as the noise of the atom number ΔN_{atoms}. The atom number is calculated as in equation (2.15) and the noise correspondingly as $\Delta N_{atoms} = A/\sigma_0 \cdot \Delta od$.

The results for the Signal-to-Noise Ratio are similar for all pulse durations and show a maximum at around $I_0 \approx 4\,I_{sat}$. However, as can be seen in figure 3.19 the atom number

still decreases measurably for small intensities and is only constant for intensities of the imaging laser above $I_0 \approx 5\, I_{sat}$ corresponding to a power factor used in the experiment of *power factor* ≈ 1.8. The *power factor* is a measure for the imaging power used in the programming of the experiment and therefore mentioned at this point. Therefore, the optimal regime for imaging is not directly at the minimum of the noise, but at around *power factor* ≈ 2. Thus, the preferred regime of the imaging is identified to be at around $10\mu s$ and *power factor* ≈ 2.

Chapter 4

1D-Model

The motivation for performing a 1D modelling of the BEC absorbing light, was to gain a better qualitative understanding of the multiple scattering effects in the cloud, making it possible to interpret the observed dependence of I_{sat}/σ_{sat} on the density profile of the atoms. The model is based on the work of Veyron et al. [4],[7].

4.1 Simulation Method

In the simulation the set of coupled differential equations defined in equation (2.27) is solved numerically. The result is an intensity profile of the coherent probe beam light s_c, and the scattered lights co- (s_i^+) and counterpropagating to the probe beam direction (s_i^-) along the z-axis. The simulation is performed as follows: The three coupled differential equations are solved numerically with the Euler method along the only direction (z-direction, from z_{min} to z_{max} in steps of dz). The initial conditions are based on the physical reality of the imaging, assuming no atoms at z_{min} and z_{max}:

- No scattered light in negative z-direction at z_{max}, $s_i^-(z_{max}) = 0$
- No scattered light in positive z-direction at z_{min}, $s_i^+(z_{min}) = 0$
- Coherent light intensity at z_{min} is the full initial imaging intensity, $s_c(z_{min}) = s_{c,0}$

The equations are now solved in an iterative process, leading to a self-consistent solution. At step $l = 0$, the coherent intensity is calculated without considering scattering effects ($s_i^{+/-} = 0$).
Then, at step l, the equation for $s_i^{+,l}(z)$ is solved with $s_c^{l-1}(z)$ and $s_i^{-,l-1}(z)$ as input. A similar calculation is done for $s_i^{-,l}(z)$, using $s_c^{l-1}(z)$ and $s_i^{+,l-1}(z)$. The solutions for $s_i^{+/-,l}(z)$ are now inserted in the equation for $s_c^i(z)$. This iterative process is performed until no change between successive steps is observed. At this point, a self-consistent solution is reached, and the equations are considered solved. The whole process is taken from the work of Veyron et al. in [4]. The solutions for different initial conditions are shown in figure 4.1, and depict the expected behaviour of an absorption of the imaging light and redistribution of the light as incoherently scattered light.

In this one-dimensional model, the density distribution is of a Gaussian form along the z-direction. The width of the Gaussian is based on previous experimental results (see [10])

to be $\sigma_z \approx 0.4\mu m$. The free parameter of the density distribution centred around $z = 0$ is the amplitude of the normalized Gaussian. To compare the model to the experimental results, the optical density along the z-axis is used as a parameter. The normalization and amplitude of the Gaussian is then given by the prefactor:

$$n_0(od) = \frac{od}{\sigma_0\sqrt{2\pi\sigma_z^2}}, \tag{4.1}$$

where σ_0 is again the cross section defined in (2.8) used to relate the optical density to a column density as in equation (2.13).

In this way the only free parameters left for the model are the initial imaging intensity $s_{c,0}$, the optical density od, the single-atom cross section $\alpha_{SA} = 2$ for the here used multi-level system (see section 2.3.1) and the isotropic cross section is either $\alpha_{iso} = 1$ for σ^- polarized light or $\alpha_{iso} = 2.12$ for isotropically polarized incoherent light. The values for α_{iso} are taken from [4].

4.2 Results of the Simulation

Figure 4.1 shows the three different intensities of the coherent light and the two scattered lights as a function of z-direction for different initial intensities (columns) and optical densities (colour shade). In the background, the assumed density distribution along the z-axis is depicted with arbitrary scale (not showing the difference in optical densities) to compare the shape of the curves with the atomic density distribution.
The behaviour of three different initial intensities normalized by the theoretical saturation intensity $s_{c,0} = \frac{I_0}{I_{sat}}$ is studied. At the three different initial intensities, the coherently and incoherently scattered intensity is depicted over the length of the cloud for different optical densities of the atoms.

At all values of $s_{c,0}$ the expected decrease of the coherent light as it passes through the cloud is observed, because some light is absorbed by atoms and re-scattered. Similarly, an increase in the negative scattered incoherent light s_i^- is observed, due to more light being absorbed and re-emitted. The maximum amount of the positive scattered light also increases with higher optical density as a result of this scattering. At high optical densities, the amount of incoherent light in the positive z-direction decreases, as more of this light is re-scattered into the negative direction as is added from the opposite process and the first scattering of coherent light.

Because the simulations are performed at multiple optical densities od, they can be used to infer $\alpha(od)$. The coherent and incoherent light that leave the cloud to positive z-direction ($s_c(z_{max}) + s_i(z_{max})^+$) are representative of the intensity of the atom image, while the initial light intensity $s_{c,0}$ can be compared to the initial intensity experimentally extracted form the reference image. To gain a quantitative result, the scattered light has to be corrected for the solid angle of the imaging system $\Omega = 0.13$ calculated from the numerical aperture ($NA = 0.5$) ([10]). The value of α can be calculated by inverting the

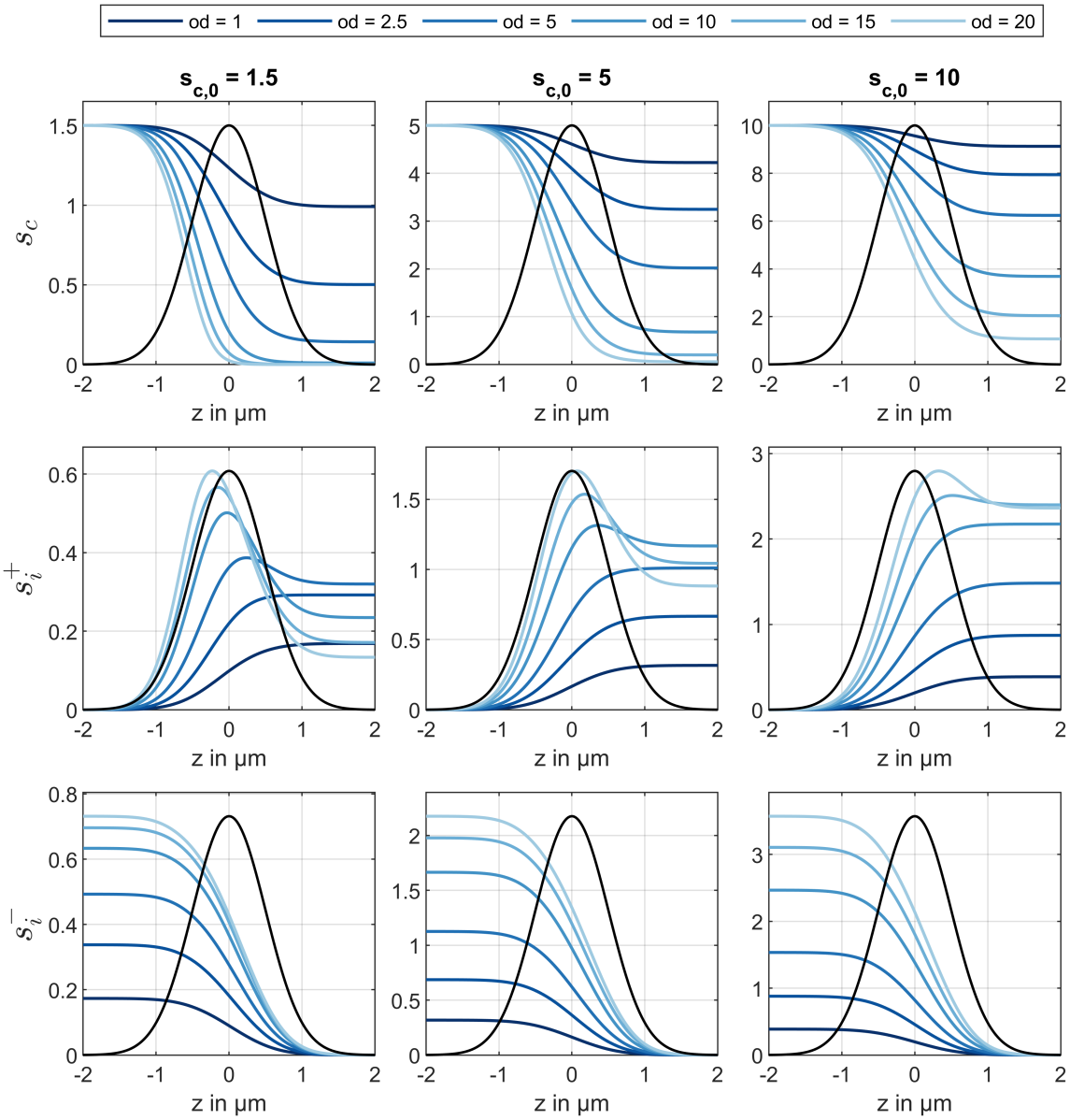

Figure 4.1: **1D model for imaging intensities of $s_{c,0} = 1.5, 5, 10$ and different optical densities.** For three initial imaging intensities the simulation of the coherent light s_c, the light scattered in negative z-direction s_i^- and the light scattered in positive z-direction s_i^+ is shown over z. The width of the Gaussian density is assumed to be $\sigma_z = 0.4\,\mu m$. All the simulations are performed for different total optical densities of the cloud, shown in different shades of blue. Figure inspired by [4].

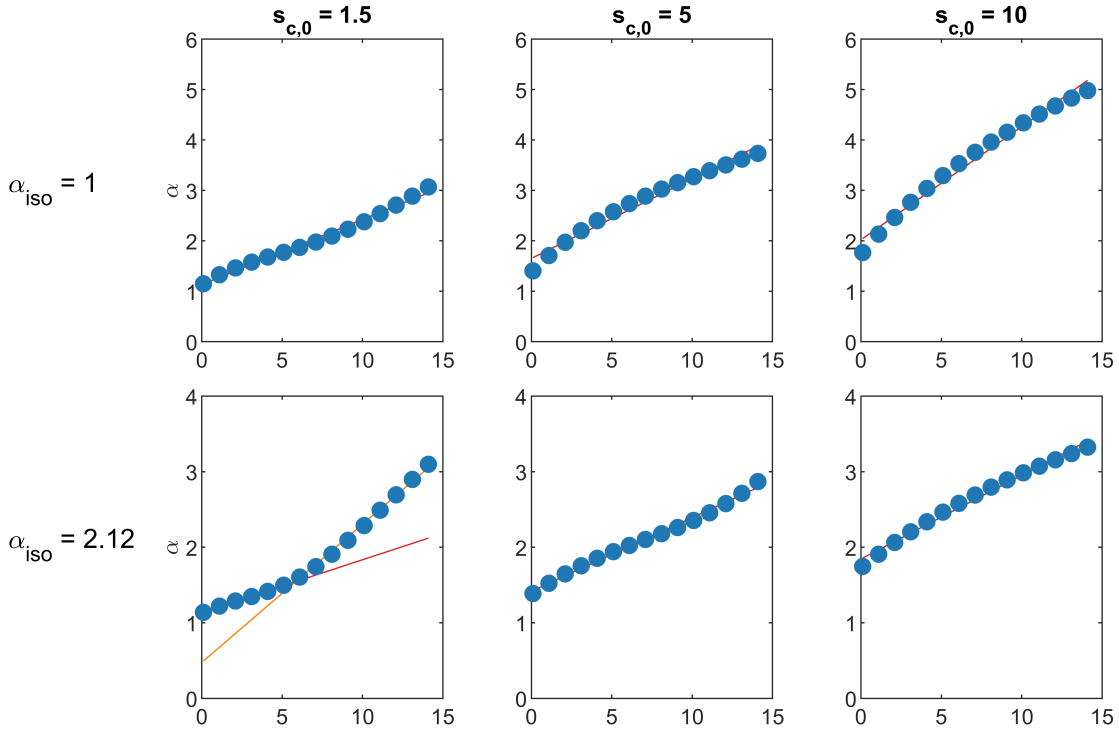

Figure 4.2: **Results from 1D simulations for $\alpha(od)$ at different imaging intensities and two values of α_{iso}.** Based on the simulations presented in figure 4.1 the corresponding values of $\alpha(od)$ are calculated. The simulations were now also done for different values of $\alpha_{iso} = 1, 2.12$ describing a smaller probability for reabsorption of rescattered light based e.g. on polarization, but could also be considered to account for losses of scattered photons. It can be seen that the linear assumption of $\alpha(od)$ is in good approximation valid for $s_c > 5$. This would correspond to most of the imaging intensities used for the calibrations.

equation of the optical density (Eq. (2.14)):

$$\alpha = \frac{-od - [s_c(z_{max}) + s_i^+(z_{max})\Omega\alpha_{iso} - s_{c,0}]}{ln\left(\frac{s_c(z_{max})+s_i^+(z_{max})\Omega\alpha_{iso}}{s_{c,0}}\right)}. \tag{4.2}$$

The occurrence of α_{iso} in the equation is to make s_i^+ comparable to the intensity given by $s_c = I_0/I_{sat}$ while $s_i = I_{+/-}/(\alpha_{iso}I_{sat})$. The results of this calculation are depicted in figure 4.2 again for three different values of $s_{c,0}$, but in addition, also the parameter α_{iso} was varied and the results of two values of α_{iso} are displayed. The meaning of α_{iso} can be understood in two ways: first, by the primary motivation as accounting for a smaller probability of absorption by a changed (isotropic) polarization of the scattered photons. Secondly, it could mimic the loss of light in the 2D/3D case from the considered *column* of atoms using α_{iso} as an effective attenuation factor. This second idea is not tried in this project, but could be used when transferring the model to the 2D/3D case.

4.3 Conclusions from 1D Simulation

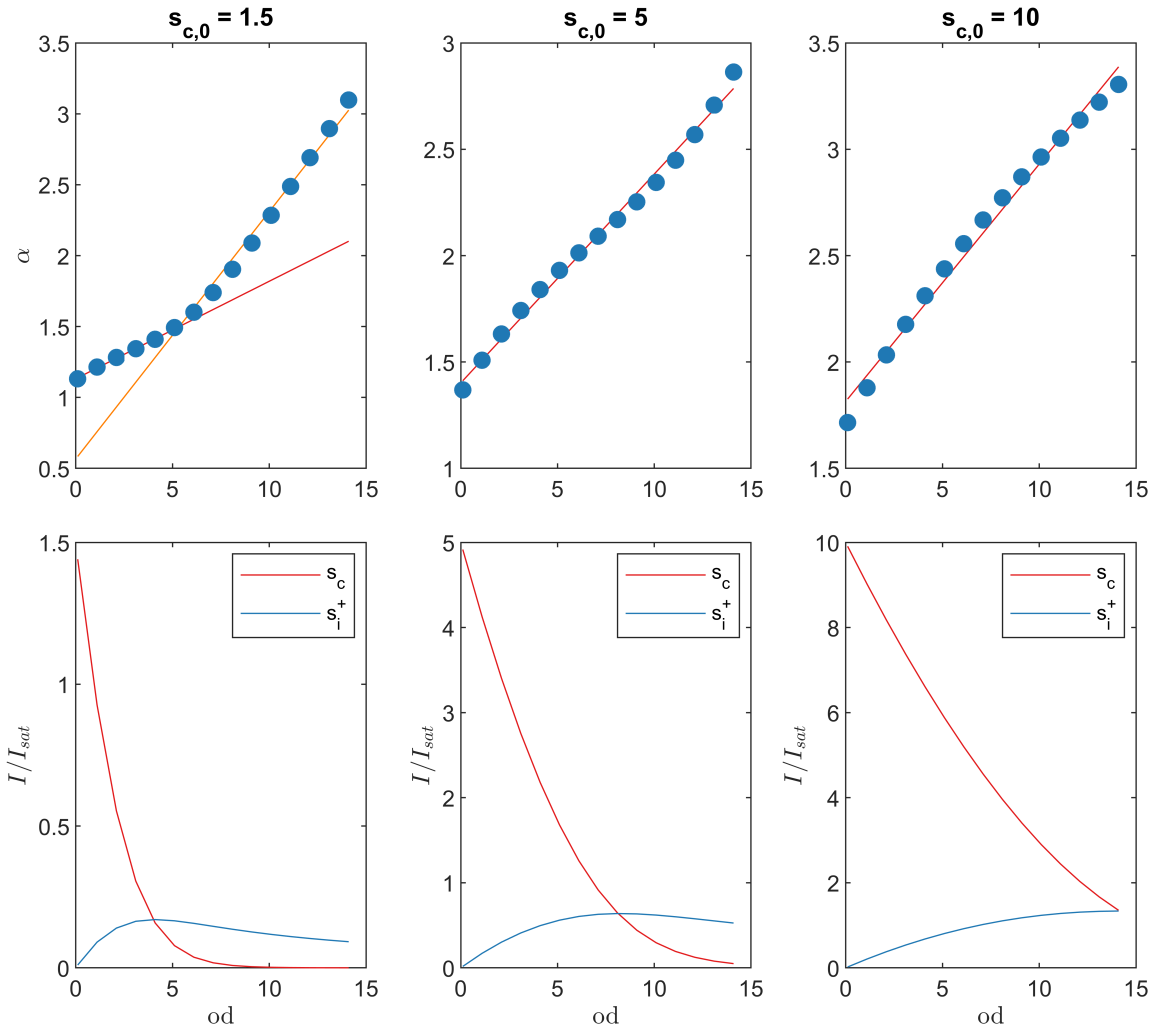

Figure 4.3: **1D model calculating $\alpha(od)$ with comparison to $s_i^+(z_{max})$ and $s_c(z_{max})$ as a function of od.** In the upper plots, $\alpha(od)$ is again shown based on the 1D-simulation for different initial imaging intensities of $s_c = 1.5, 5, 10$, below the results of $s_c(z_{max})$ and $s_i^+(z_{max})$ are plotted. The plots are all produced with $\alpha_{iso} = 2.12$. The shift of the turning point of $\alpha(od)$ to higher od with increasing $s_{c,0}$ seems to coincide with a higher amount of light being re-scattered in positive z-direction.

The results produced by the simulation have clear quantitative differences to the 2D/3D-case of the experiment, but the results can verify the assumption of a linear relation used to describe $\alpha(od)$ in most parameter regimes of imaging intensity and optical density. The now constant parameter of $s_{c,0}$ is comparable to the case of $I_0 = \text{const.}$ which is not realizable when performing the calibration, because the change in absorbed intensity needs to be studied for several imaging intensities. These fundamental differences make the quantitative comparison of the trajectories of $\alpha(od)$ to the calibrations performed with constant N_{abs} or constant t_{pulse} difficult. The simulation could be modified to resemble the case of constant N_{abs}, this was not done in this project, because a qualitative comparison was the aim of performing this simulation. A quantitative comparison to

the experimental calibration was already not possible, because of the differences to the 2D-case.

However, for all intensities and optical densities that were considered in the simulation, the validity of the linear approximation for $\alpha(od)$ is qualitatively verified. An interesting observation is a residual curvature of $\alpha(od)$, clearly visible for $s_{c,0} = 1.5$. Especially the regime of low densities (and od) shows this non-linear behaviour, whereas the higher optical densities retain the linear relation. This curved shape was also observed for the calibration based on the constant N_{abs} as discussed in section 3.3, as α is larger than the linear fit at small od, and for the calibration based on the constant t_{pulse} as discussed in section 3.4, as α is smaller than the linear fit at small od, precisely shown in figure 3.4 and 3.7.

In the case of the 1D-model, the linear fit seems to better describe the trajectory of $\alpha(od)$ at higher imaging intensities $s_{c,0}$. Because typical initial intensities used in the calibration are on average of the order $s_c \approx 8$ and vary between $1.4 < s_c < 14$, the results provided by the simulation approve the linear assumption made for $\alpha(od)$. Especially, for experimentally relevant imaging intensities, based on optimal signal-to-noise $s_c > 5$ (see section 3.8), the linear trajectory of $\alpha(od)$ is qualitatively validated by the results of the simulation.

The occurrence of this deviation from the linear functional form is studied in more detail in figure 4.3. In this figure, the simulated calibration for $\alpha_{iso} = 2.12$ is again shown at three different imaging intensities $s_{c,0}$. The plots below show the simulated intensities s_c (red) and s_i^+ (blue) leaving the cloud in positive z-direction (at position z_{max}). The turning point of $\alpha(od)$ (with a good linear estimation for the points above and below) seems to coincide with a higher portion of the light leaving the atomic cloud in positive z-direction being re-scattered light, while most of the initial incident laser light is being absorbed. In this regime, the description of the absorption probably deviates from the model usually considered for the absorption. In the experiment a considerable amount of coherent light is expected to leave the cloud in positive z-direction thus, the measurements are mostly far off all laser intensity being absorbed by the atoms.

The agreement of the experimental data and the 1D simulation is fundamentally limited by experimental effects that are not present in the simulation. To extract data for multiple optical densities simultaneously, a two-dimensional profile with a radial density gradient was used. There, the cross-talk between neighbouring pixels, which are a realization of the 1D system with a given od, could be asymmetric as a result of the gradient in density. Also, the comparison to a calibration based on N_{abs} makes understanding the functional form of $\alpha(od)$ more involved, because the value of N_{abs} is only estimated globally over the cloud and not for every density region individually. Finally, the concurrent variation of imaging pulse duration t_{pulse} and imaging power I_0 to remain at a fixed value of N_{abs} makes the comparison to the simulated data less valid. The general linear relation of $\alpha(od)$ from the simulations can also be observed in the experimental calibrations. Although, the calibrations performed with a linear density profile deviate in the manner described above from the linear assumption, similar to the deviation observed in the simulation for low imaging intensities. The calibration made for both cases (constant

N_{abs} and t_{pulse}) based on a homogenous density profile provides a better estimate of a linear trajectory, as can be seen in figures 3.10 and 3.11.

The 1D-model provides some interesting insights, supporting the assumption of a linear behaviour of $\alpha(od)$ based on the effect of multiple scattering. The quantitative results, as well as reasons for the deviation from a linear relation, are difficult to directly compare with experimental calibration results. To make the simulation more comparable, first the case of constant N_{abs} should be reproduced in the simulation, and second the simulation should be performed for a 2D density distribution. This could be done by estimating the probability of scattered photons being reabsorbed by the surrounding atoms. For high atomic densities it could be possible to use a model of the diffusion of light in the x-y-plane or use a Monte Carlo simulation to simulate the paths of the photons. This would provide a more realistic description of the scattering process and the resulting light intensity.

Chapter 5

Conclusion

This thesis demonstrates the successful implementation of a more accurate measurement of density distributions in a BEC using absorption imaging. This improved calibration incorporates multiple scattering of photons, which results in density-dependent effects that were previously not considered. Beyond the practical result of a better calibration, steps were taken towards a better understanding of the multiple scattering processes by performing several measurements for different density distributions in the atomic cloud and comparing the results with a 1D-model, built to match the case of the experiment. The results of this thesis are summarized in the following:

The method for a density-dependent calibration of the absorption imaging, presented by Vibel et al. in [3], was applied to the case of the experiment, with measurements at different imaging intensities and imaging laser pulse durations t_{pulse}. A relation for the saturation parameter $\alpha(od)$ was derived for two different cases: Constant number of scattered photons per atom N_{abs} and constant imaging pulse duration t_{pulse}. Both calibrations show a similar behaviour of $\alpha(od)$ with differences in the exact trajectory, but with an approximately linear behaviour of $\alpha(od)$ and values in a similar regime of $\alpha > 2$.

For both calibrations (constant N_{abs} and constant t_{pulse}) trends of the parameters of the linear relation $\alpha = \alpha_0 + \alpha' \cdot od$ were studied. The calibration method presented in [3] (and previous calibrations) uses a constant N_{abs} to minimize the influence of the Doppler shift on the atoms. However, the N_{abs} in a cloud of atoms is difficult to control experimentally and makes the understanding of the underlying processes more complex. The calibration based on constant imaging pulse duration t_{pulse} has several advantages compared to the calibration based on N_{abs} and will therefore be implemented in the experiment. Importantly, for the local calibration with constant t_{pulse} only experimentally useful parameters (imaging intensity and imaging pulse duration t_{pulse}) need to be considered. The applied local calibration is shown to correct for underestimations of the atom number at high densities and overestimations at low densities, as expected due to multiple scattering effects.

While $\alpha(od)$ is well described linearly, some non-linear behaviour is apparent both in the experiment and the theoretical results of the 1D-model. The observed effect is in the theory of the model, but the explanation remains an outstanding challenge. In the 1D

case, it seems to coincide with the ratio of multiple scattered light to imaging light not absorbed by the atoms. This observation was not further investigated but demands more experimental and theoretical investigation.

By optimizing the imaging parameters to maximize the signal-to-noise ratio, this calibration can now be integrated into the experiment, providing a more accurate and consistent atom number estimation. This advancement enhances the reliability of future density measurements and lays the groundwork for further investigations into multiple scattering effects and density-dependent behaviours.

Topics for further investigation could be the following:

- This project demonstrates that the absorption response of the atoms is density dependent and is thus also dependent on the density profile realized in the atomic cloud. In the calibration discussed here, the effect of density gradients was not considered but should be incorporated in future calibrations. An idea for a calibration applicable to arbitrary density distributions could be to take the α-values in surrounding regions of one pixel into consideration when calculating the final α for this pixel. This would include the influence of surrounding regions at different densities on the absorption behaviour of the atoms in the pixel. The effect of the edges of the cloud could be considered similarly.

- A more quantitative analysis of the influence of the Doppler shift on the absorption imaging signal should be conducted. This can be done by considering the Doppler shift as a resonance shift in the theoretical model. To evaluate the influence more scattered photons have on the absorption behaviour of the atoms, the resulting correction could lead to a more stable atom number across different imaging pulse durations. This may be derived from the work presented in [16] on the Doppler shift and effective scattering cross section.

- At the highest densities realized in the experiment, the influence of light diffusion could have an impact on the absorption imaging. This could be considered in the experiment following the work presented in [17]. This work provides another argument towards the considerable influence of multiple scattering at the upper limit of densities used in the experiment. This model of diffusion could then be used for a 2D/3D model of multiple scattering in the cloud at high densities. An alternative for expanding the 1D-model would be using Monte Carlo simulations for the transmission of photons, including the effect of rescattering, similar to the simulations performed in [18].

- Changes in the saturation behaviour of N_{abs} with the imaging intensity depending on the optical density as presented in section 3.1 could be compared to the simulation performed in [15] for the number of scattered photons. This could provide insights to further understand the multiple scattering effects at different densities.

Bibliography

[1] G. Reinaudi et al. "Strong saturation absorption imaging of dense clouds of ultracold atoms". In: *Opt. Lett.* 32.21 (Nov. 2007), pp. 3143–3145. DOI: 10.1364/OL.32.003143. URL: https://opg.optica.org/ol/abstract.cfm?URI=ol-32-21-3143.

[2] Maurus Hans. "Physical Computing on a Versatile Setup for Ultra-cold Potassium". Doctoral Thesis. Heidelberg University, 2022. DOI: 10.11588/heidok.00032365.

[3] T Vibel et al. "Spatial calibration of high-density absorption imaging". In: *Journal of Physics B: Atomic, Molecular and Optical Physics* 57.14 (June 2024), p. 145301. DOI: 10.1088/1361-6455/ad53ae. URL: https://dx.doi.org/10.1088/1361-6455/ad53ae.

[4] Romain Veyron et al. "Quantitative absorption imaging: The role of incoherent multiple scattering in the saturating regime". In: *Phys. Rev. Res.* 4 (3 July 2022), p. 033033. DOI: 10.1103/PhysRevResearch.4.033033. URL: https://link.aps.org/doi/10.1103/PhysRevResearch.4.033033.

[5] Harold J. Metcalf and Peter Van der Straten. *Laser Cooling and Trapping*. Graduate Texts in Contemporary Physics. Springer Science & Business Media, 1999, p. 323. ISBN: 0387987479, 9780387987477.

[6] T. G. Tiecke. "Feshbach resonances in ultracold mixtures of the fermionic quantum gases 6Li and 40K". PhD thesis. University of Amsterdam, 2009.

[7] R. Veyron et al. "Effective two-level approximation of a multilevel system driven by coherent and incoherent fields". In: *Phys. Rev. A* 105 (4 Apr. 2022), p. 043105. DOI: 10.1103/PhysRevA.105.043105. URL: https://link.aps.org/doi/10.1103/PhysRevA.105.043105.

[8] Maurus Hans et al. "High signal to noise absorption imaging of alkali atoms at moderate magnetic fields". In: *Review of Scientific Instruments* 92.2 (Feb. 2021), p. 023203. ISSN: 0034-6748. DOI: 10.1063/5.0040677. eprint: https://pubs.aip.org/aip/rsi/article-pdf/doi/10.1063/5.0040677/15779999/023203_1_online.pdf. URL: https://doi.org/10.1063/5.0040677.

[9] B. R. Mollow. "Power Spectrum of Light Scattered by Two-Level Systems". In: *Phys. Rev.* 188 (5 Dec. 1969), pp. 1969–1975. DOI: 10.1103/PhysRev.188.1969. URL: https://link.aps.org/doi/10.1103/PhysRev.188.1969.

[10] Celia Viermann. "Cosmological particle production and curved spaces in an ultracold quantum gas". Doctoral Thesis. Heidelberg University, 2022. DOI: 10.11588/heidok.00031490.

[11] Jiri Etrych et al. "Pinpointing Feshbach resonances and testing Efimov universalities in 39-K". In: *Phys. Rev. Res.* 5 (1 2023), p. 013174. DOI: 10.1103/PhysRevResearch.5.013174. URL: https://link.aps.org/doi/10.1103/PhysRevResearch.5.013174.

[12] G. Breit and I. I. Rabi. "Measurement of Nuclear Spin". In: *Phys. Rev.* 38 (11 Dec. 1931), pp. 2082–2083. DOI: 10.1103/PhysRev.38.2082.2. URL: https://link.aps.org/doi/10.1103/PhysRev.38.2082.2.

[13] E. P. Gross. "Structure of a Quantized Vortex in Boson Systems". In: *Il Nuovo Cimento (1955-1965)* 20.3 (1961), pp. 454–477. ISSN: 1827-6121. DOI: 10.1007/BF02731494. URL: https://doi.org/10.1007/BF02731494.

[14] L. P. Pitaevskii. "Vortex Lines in an Imperfect Bose Gas". In: *Journal of Experimental and Theoretical Physics* 13 (1961), pp. 451–454.

[15] Finn Schmutte. *Closed Optical Cycle Scheme for Absorption Imaging of 39-K Atoms at Intermediate Magnetic Field Strengths*. Bachelor's Thesis. 2021. URL: https://www.kip.uni-heidelberg.de/Veroeffentlichungen/download.php/6867/temp/4572.pdf.

[16] Maximilian Emanuel Manfred Kob. *High intensity absorption imaging scheme for a Dysprosium quantum gas*. Bachelor's thesis. Aug. 2023. URL: https://www.pi5.uni-stuttgart.de/documents/abgeschlossene-arbeiten/2023-Kob-Maximilian-High-intensity-absorption-imaging-scheme-for-a-Dysprosium-quantum-gas-BSc.pdf.

[17] Antoine Glicenstein et al. "In Situ Measurements of Light Diffusion in an Optically Dense Atomic Ensemble". In: *Phys. Rev. Lett.* 133 (23 Dec. 2024), p. 233401. DOI: 10.1103/PhysRevLett.133.233401. URL: https://link.aps.org/doi/10.1103/PhysRevLett.133.233401.

[18] L Chomaz et al. "Absorption imaging of a quasi-two-dimensional gas: a multiple scattering analysis". In: *New Journal of Physics* 14.5 (May 2012), p. 055001. DOI: 10.1088/1367-2630/14/5/055001. URL: https://dx.doi.org/10.1088/1367-2630/14/5/055001.

Acknowledgements

First and foremost, I would like to thank Prof. Markus Oberthaler for giving me the opportunity to work on this incredible project. His enthusiasm for research, ultra-cold atom experiments, and physics in general is truly contagious. His frequent exclamations of "super cool" in meetings were always a great source of motivation. Also I greatly thank Prof. Selim Jochim for co-examining the thesis.

I am deeply grateful to the BECK experiment team— Jelte Duchene, Louis Evans, Elinor Kath, Nikolas Liebster, Marius Sparn and Dr. Helmut Strobel—for welcoming me, providing invaluable guidance and support, and fostering a fantastic atmosphere both in and beyond physics. Working with you has been an absolute pleasure, and I have learned so much from your passion and expertise.

A special thank you goes to Nikolas Liebster, whose initiative and guidance were instrumental in shaping this project. His willingness to answer my questions, discuss results, and explore new ideas was invaluable. This project would not have been possible without his insight, dedication, and contagious enthusiasm for research. I greatly enjoyed working alongside him over the past months.

I would also like to thank the entire Matterwave group for their great company and shared love of coffee. Speaking of which, a heartfelt thanks to coffee itself—without an adequate daily dose, this project might not have been possible.

Declaration

Ich versichere, dass ich diese Arbeit selbstständig verfasst und keine anderen als die angegebenen Quellen und Hilfsmittel benutzt habe. Für die Überprüfung von Rechtschreibung und Grammatik einzelner Sätze wurde ChatGPT und DeepL verwendet. Die Datenanalyse wurde vollständig ohne die Unterstützung von KI durchgeführt.

I certify that I have written this thesis independently and have not used any sources or aids other than those specified. ChatGPT and DeepL were used to check the spelling and grammar of individual sentences. The data analysis was carried out entirely without the support of AI.

Heidelberg, den 03.04.2025

Philipp Martin Weingardt